Linking African easterly wave activity with equatorial waves and the influence of Rossby waves from the Southern Hemisphere

Article

Accepted Version

The DOI for this manuscript is doi: 10.1175/JAS-D-17-0184.1

Linking African Easterly Wave activity with equatorial waves and the influence of Rossby waves from the Southern Hemisphere

Gui-Ying Yang[1, 2], John Methven[2], Steve Woolnough[1, 2], Kevin Hodges[2] and Brian, Hoskins[2]

1. National Centre for Atmospheric Science, UK

2. Department of Meteorology, University of Reading, UK

Submit to JAS

Revised in Feb. 2018

*Corresponding Author address:
Gui-Ying Yang
Department of Meteorology
University of Reading
Earley Gate
Reading RG6 6BB, UK
Email: g.y.yang@reading.ac.uk

Abstract

A connection is found between African easterly waves (AEWs), equatorial westward-moving mixed Rossby-gravity (WMRG) waves and equivalent barotropic Rossby waves (RWs) from the Southern Hemisphere (SH). The amplitude and phase of equatorial waves is calculated by projection of broad-band filtered ERA-Interim data onto a horizontal structure basis obtained from equatorial wave theory. Mechanisms enabling interaction between the wave types are identified. AEWs are dominated by a vorticity wave which tilts eastwards below the African Easterly Jet and westwards above: the tilt necessary for baroclinic wave growth. However, a strong relationship is identified between amplifying vorticity centres within AEWs and equatorial WMRG waves. Although the waves do not phase-lock, positive vorticity centres amplify whenever the cross-equatorial motion of the WMRG wave lies at the same longitude in the upper troposphere (southwards flow) and east of this in the lower troposphere (northwards flow). Two mechanisms could explain the vorticity amplification: vortex stretching below the upper-tropospheric divergence and ascent associated with latent heating in convection in the lower-tropospheric moist northwards flow.

In years of strong AEW activity, SH and equatorial upper-tropospheric zonal winds are more easterly. Stronger easterlies have two effects: i) they Doppler shift WMRG waves so that their period varies little with wavenumber (3-4 days) and ii) they enable westward-moving RWs to propagate into the tropical wave guide from the SH. RW phase speeds can match those of WMRG waves, enabling sustained excitation of WMRG. The WMRG waves have an eastwards group velocity with wave activity accumulating over Africa and invigorating AEWs at similar frequencies through the vorticity amplification mechanism.

Key words: AEWs, equatorial waves, Rossby waves, wave interaction, vortex stretching, phase speed match, tropical wave guide

1. Introduction

African Easterly Waves (AEWs) are lower tropospheric disturbances initiating, growing and propagating westwards across northern Africa into the tropical Atlantic and sometimes continuing across to the Caribbean Sea (Burpee 1972; Avila and Pasch 1992). AEWs usually appear in May and activity continues until October or November. They dominate precipitation over West Africa, modulating rainfall through the initiation and organization of mesoscale convective systems and squall lines (Carlson 1969b; Duvel 1990; Diedhiou et al.1999; Fink and Reiner 2003; Mekonnen et al. 2006; Crétat et al. 2015) which produce intense precipitation. Mesoscale convective systems account for over 80% of total annual rainfall in the Sahel (e.g.,Laurent et al. 1998 and Mathon et al. 2002). AEWs exhibit strong interannual variability: a major influence on the occurrence of precipitation and climate impacts across the region. Here, a key aim is to identify the physical mechanisms which are important to AEW amplification, propagation and the variability in wave activity.

AEWs are observed to have a period of 3-5 days (Burpee 1972) and a westward phase speed of about 8-10 ms^{-1} (Reed et al. 1977; Price et al. 2007). Their typical zonal wavelength has been reported to be 2000-2800 km (zonal wavenumber k=14-19) in early studies (e.g., Carlson 1969a; Burpee 1974, 1975; Reed et al. 1977) but to be longer (3000-5000km, k=8-13) in some later studies (e.g., Diedhiou et al. 1999 and Kiladis et al. 2006).

Cyclonic vorticity centres within AEWs seed a large proportion of tropical cyclones over the North Atlantic (Frank 1970; Avila and Pasch 1992; Landsea 1993; Landsea et al. 1998; Thorncroft and Hodges 2001), with about 60% of Atlantic tropical cyclones and weak hurricanes originating from AEWs and approximately 85% of intense hurricanes developing from AEWs (Landsea 1993). It has also been suggested that nearly all of the tropical cyclones that occur in the East Pacific can be associated with AEWs propagating from the Atlantic (Serra et al, 2010) and possibly traced back to Africa (Avila and Pasch 1995).

Therefore understanding the amplification, intensity and phase speeds of AEWs is important for weather forecasting in the tropics and extratropics.

However, despite a long history of research on AEWs, understanding of the mechanisms behind the dynamics and variability of AEWs is still qualitative and incomplete. Furthermore, there are severe deficiencies in the simulation of the initiation, amplitude and phase speeds of AEWs in both numerical weather prediction (Berry et al. 2007; Agustí-Panareda et al.2010) and climate simulations. There are a number of studies relating interannual variability in AEWs to the global circulation of the atmosphere. For example, Nicholson (2009) argued, using one wet and dry year across West Africa, that the strongest difference in the large-scale flow between the years was seen in the upper troposphere, rather than in the lower troposphere at the level of the African Easterly Jet. The year with stronger precipitation had stronger monthly mean ascending motion in the West African rain belt, stronger divergent outflow (equatorward flow south of the rain belt) and a stronger Tropical Easterly Jet (in the equatorial upper troposphere). These observations are all consistent with a stronger meridional circulation (local Hadley cell) across Africa. However, the link with AEW activity was unexplained.

Elsewhere across the tropics, envelopes of active convection and the location of convective systems are also frequently observed to be related to the structure of large-scale waves. Equatorial waves with an internal first baroclinic mode structure in the vertical including the Kelvin, mixed Rossby-gravity and Rossby waves identified from different branches of the dispersion relation derived by Matsuno (1966), are fundamental components of the tropical climate system and have been shown to dominate precipitation variability across tropical ocean basins (e.g., Wheeler and Kiladis 1999; Molinari 2004; Yang et al.2007a; Yang and Hoskins 2013).

Equatorial waves are trapped near the equator but can propagate in the zonal and vertical directions. Yang et al. (2007a, 2011, 2012) and Yang and Hoskins (2013, 2016) found that the tropical winds and the geopotential anomaly from meteorological analysis data project strongly onto the equatorial wave modes based on the theory of a resting atmosphere. Figure 1 shows the horizontal structures of the three gravest (lowest meridional wavenumber n) westward-moving equatorial wave modes: the n=0 westward-moving mixed Rossby-gravity (WMRG) wave and n=1 or 2 Rossby waves (denoted R1 and R2). It is seen that although they are equatorially trapped, they can have strong rotational and divergent motions off the equator at a distance determined by the horizontal structure of each mode and a single "trapping scale" (see Eq. 5). A major theoretical challenge is that the zonal flow across the tropical Atlantic and Africa (north of the equator) is strongly sheared with the existence of the African Easterly Jet (AEJ - peaking at 600 hPa near 10-20°N) and Tropical Easterley Jet (TEJ - around 200 hPa nearer the equator). The shear on the AEJ is thought to be essential to the existence of AEWs through baroclinic and barotropic shear instability (Hall et al 2006; Cornforth *et al*, 2017). In contrast, equatorial wave theory does not deal with shear which is why the horizontal modes (Fig.1) are untilted in the zonal direction. Nevertheless, the equatorial wave structures form a useful orthogonal basis where the horizontal velocity components and geopotential are coherent. A key modification resulting from vertical wind shear is that the data projected onto the horizontal structures at each level reveals coherent wave modes that are tilted with height (e.g., Zhang and Webster 1989; Yang et al. 2007a, 2011, 2012). Regions of active/inactive convection are also determined by the dynamics of the large-scale waves.

Across Africa and the Atlantic, the meridional shear in the zonal flow is much stronger than elsewhere in the tropics due to the AEJ. Therefore, the structures of any equatorially-trapped large-scale waves must overlap with regions of strong shear. Although equatorially-

trapped waves obtained as normal mode solutions to the shallow water equations on a uniform flow are untilted, orthogonal and non-interacting, these properties are lost in the presence of shear in the zonal flow. Vertical wind shear also enables interaction between Rossby and gravity waves, as shown for example in a two layer model by Sakai (1989). The aim of this study is to identify interactions between AEWs and equatorially-trapped waves and their effects on AEW variability. A particular focus is on AEW interaction with WMRG wave activity propagating along the equator and excitation of those waves by equivalent barotropic Rossby waves from the Southern Hemisphere.

The paper is organized as follows. Section 2 describes the re-analysis data and methods used for vorticity tracking, spatio-temporal filtering, spatial projection onto wave components and the regression technique. Section 3 presents a climatology of the distribution of AEW intensity, both spatially, through tracking positive vorticity centres within AEWs, and also in zonal wavenumber-frequency space. The inter-annual variability is also examined. Section 4 presents a case study of AEWs occurring during the active 1995 summer season and the associated tropical cyclogenesis events. Re-analysis data is projected onto the horizontal structures of equatorial wave components (on pressure levels spanning the troposphere) and the link between westward propagating wave structures and the vorticity centres of AEWs is examined in detail. In Section 5, the case study findings are extended to the entire re-analysis period by calculating average horizontal and vertical structures relative to the AEW vorticity centres using a lag regression analysis. Section 6 examines the differences in equatorial wave activity and the seasonal-mean flow between years of strong and weak AEW activity. Dynamical mechanisms linking the different waves are identified using the theory for wave propagation on the observed seasonal-mean flow. Conclusions are drawn in Section 7.

2. Data and methodology

a. Data

125 The data used in this study are from the European Centre for Medium-Range Weather
126 Forecasts Re-Analysis, ERA-Interim (data available from ECMWF; Dee et al. 2011). The
127 fields used are the horizontal winds (u, v) and the geopotential height (Z) for the period from
128 1979 to 2010. The fields are available 6-hourly with horizontal resolution of about 0.7° and at
129 37 pressure levels from 1000 to 1 hPa. The proxy used for tropical convection is NOAA
130 interpolated daily outgoing longwave radiation (OLR) for the period from 1979 to 2010
131 (Liebmann and Smith 1996).
132 The troughs of AEWs can be tracked by identifying their characteristic positive
133 vorticity centres at the level of the AEJ (600 hPa). In this study, the vorticity centres are
134 tracked using the methodology of Thorncroft and Hodges (2001) and Hopsch et al. (2007).
135 The vorticity field used is spectrally filtered, where the total wavenumbers equal or smaller
136 than 5 are removed and the field is truncated to T42 and the spectral coefficients tapered to
137 suppress Gibbs oscillations. The tracks of positive vorticity centres at 600 hPa with amplitude
138 larger than $0.5*10^{-5}$ s^{-1} are used to represent the phase propagation of AEWs.

139 *b. Basic equatorial wave theory and identification of equatorial waves from data*

140 Following Matsuno (1966) and Gill (1980, 1982), equatorial wave theory is based on
141 linearization about a resting atmosphere and separation of the vertical structure from that in the
142 horizontal. The horizontal and temporal behavior of the u, v and Z satisfy the linearized shallow
143 water equations with gravity wave speed c, the separation constant from the vertical structure
144 equation that can also satisfy relevant surface and upper boundary conditions. This is possible
145 only for discrete values of the separation constant, $c_e = NH/m\pi$, where m is the vertical mode
146 number, H is the height of the tropopause and it is assumed that the tropopause acts as a rigid
147 lid.
148 For the horizontal equations, the representation of u, v and Z fields are of the form
149 $$\{u, v, Z\} = \{U(y), V(y), Z(y)\} \exp[i(kx - \omega t)], \quad (1)$$

where k is the zonal wavenumber and ω is the frequency. The equatorial wave solutions are most easily formulated in terms of new variables, q, r and v (Gill 1980) where

$$q = \frac{gZ}{c_e} + u,\ r = \frac{gZ}{c_e} - u \qquad (2)$$

There is the Kelvin wave solution with zero v and $\omega = k/c_e$, and there are solutions with non-zero v with the dispersion relation

$$\frac{\omega^2}{c_e\beta} - c_e\frac{k}{\omega} - \frac{c_e}{\beta}k^2 = (2n+1), \quad for\ n = 0, 1, 2 \ldots. \qquad (3)$$

where n is the meridional mode number and β is $\partial f/\partial y$. Since the Kelvin wave satisfies this relation with $n = -1$, this notation is conventionally used to label it. The Kelvin wave is eastward moving. The n=0 mode is the mixed Rossby-gravity (MRG) wave which has both eastward (EMRG) and westward-moving (WMRG) solutions. For n=1 and higher there are westward-moving equatorial Rossby waves and both eastward and westward-moving gravity wave solutions.

The meridional (y) structures of the waves satisfying the shallow water equations on the equatorial β-plane are parabolic cylinder functions:

$$D_n\left(\frac{y}{y_0}\right) = \exp\left[-\frac{1}{4}\left(\frac{y}{y_0}\right)^2\right] P_n\left(\frac{y}{\sqrt{2}y_0}\right) \quad , \qquad (4)$$

where $$y_0 = \left(\frac{c_e}{2\beta}\right)^{1/2} , \qquad (5)$$

is the meridional scale, P_n is proportional to a Hermite polynomial of order n, and the waves are trapped at the equator on a scale $y_t = \sqrt{2}\, y_0$.

Although the separation of the vertical and horizontal structures is possible for a resting atmosphere, in general the separation of variables for observed atmospheric disturbances is not possible due to shear in the zonal flow and the lack of rigid lid so that analysis in terms of vertical modes and horizontal wave structures is not strictly valid. Hence in Yang et al. (2003) a methodology to identify equatorially-trapped waves in observational data was developed. In this study no assumption about the vertical structure or dispersion

relation is made, but at each level the fields in the tropics are projected onto the different equatorial wave modes using their horizontal structures described by parabolic cylinder functions in *y* and sinusoidal variation in *x*.

Guided by basic equatorial wave theory, the parabolic cylinder function expansions are organized and described as follows:

$$
\begin{aligned}
q &= q_o D_o + q_1 D_1 + \sum_{n=1}^{n=\infty} q_{n+1} D_{n+1} \\
v &= \quad 0 \quad + v_o D_o + \sum_{n=1}^{n=\infty} v_n D_n \\
r &= \quad 0 \quad + \quad 0 \quad + \sum_{n=1}^{n=\infty} r_{n-1} D_{n-1} \\
&\qquad \uparrow \qquad \uparrow \qquad \uparrow \\
&\quad n=-1 \quad n=0 \quad n=1,2...
\end{aligned}
\tag{6}
$$

These functions form a complete and orthogonal basis, and the projections in Eq.(6) are quite general, with q_0D_0 describing the Kelvin wave, q_1D_1 and v_0D_0 describing n=0 MRG waves, and $q_{n+1}D_{n+1}$, v_nD_n and $r_{n-1}D_{n-1}$ describing $n\geq1$ equatorial Rossby waves or gravity waves. The theoretical horizontal structures of equatorial waves have been shown in a number of previous studies (e.g., Matsuno 1966; Takayabu 1994; Wheeler et al 2000 and Yang et al. 2003). The horizontal winds and divergence of the WMRG, R1 and R2 waves that are relevant to this study are illustrated in Fig.1.

It is often convenient to identify the components of the projection with their resting atmosphere labels, but it is not assumed that these are normal modes of the system. In particular, different wave components may together make up an observed structure and their relative amplitudes may vary in time. For example, if a strong wave in vorticity exists at 10-15^{o}N (typical for an AEW) but there is no disturbance in the SH at the same level, then this would project strongly onto a combination of R1 and R2 in phase in the Northern Hemisphere (NH). The two structures would then approximately cancel in the SH in both vorticity and divergence (as seen from Fig.1). This does not imply that these structures evolve just as R1

and R2 modes would on a uniform flow – indeed the AEW exists in the strongly sheared environment of the AEJ. However, as a basis the structures are useful because *u*, *v* and *Z* are consistent with propagating wave features (albeit only exact solutions in the absence of wind shear). If a strong projection of tropical winds onto an equatorially-trapped wave structure is found (as will be shown for WMRG waves) further work is required to establish whether or not this structure propagates coherently in the fashion predicted, at least qualitatively, by equatorial wave theory.

This horizontal projection technique, applied on each level independently, has been successfully employed in a number of previous observational studies for convectively coupled equatorial waves (Yang et al. 2007a,b,c), equatorial wave behaviors in different QBO phases (Yang et al. 2011, 2012) and different ENSO phases (Yang and Hoskins 2013, 2016) and has been used to validate model simulations of equatorial waves (Yang et al. 2009).

c. Statistical analysis procedures

In this study, the projection methodology described above will be used to identify equatorial waves and then connect them with AEWs using a linear regression technique. In detail the analysis method is described as follows:

i). Filter data in the wavenumber and frequency domain.

Before projection onto the equatorial structure basis, the dynamical fields *v*, *q* and *r* between 24^{o}N and 24^{o}S in the global tropical belt are separated into eastward and westward-moving components using a space-time spectral analysis which transforms data from the *x*-*t* domain into the *k*-ω domain by performing 2-D FFT in the zonal and time direction (Hayashi 1982). The data is filtered using a broad spectral domain with zonal wavenumber $-40 < k < -3$ and period of 2.5-10 days to define the westward-moving components. Note that the convention chosen here is that $\omega \geq 0$ but *k* is positive for eastward and negative for westward phase speeds (see Fig. 3). This filtering domain is wider than the 3-5 or 2-6 day filter used in

many other studies of AEWs. The lower cut-off of 2.5 days removes the diurnal cycle, and the upper cut-off of 10 days is aimed to remove intraseasonal variability. There is a gap in power spectra between periods of 10 and 20 days and other authors have used this to partition propagating equatorial waves from the Madden-Julian Oscillation (e.g., Schreck et al. 2012 used an upper cut-off of 17 days).

ii). Project westward-filtered components onto horizontal structures of equatorial waves.

The Fourier coefficients (e.g., V(y) for each k and ω) of westward-moving v, q and r are separately projected onto parabolic cylinder functions as in Eq. (6) to obtain equatorial wave modes. To do this it is necessary to first specify the meridional scale y_0 (or equivalently the trapping scale y_t) and hence the speed c_e, so that q and r can be formed from u and Z according to Eq.(2). As in previous studies (e.g., Yang et al. 2003, 2007a, b, c, 2012), y_0 =6^o (trapping scale $y_t \approx$8.4°) is used. The value of y_0 is determined from a best fit to the data, although it is found that the analysis is not sensitive to the particular value of chosen y_0 (Yang et al. 2003, 2012). From Eq. (5), c_e is determined to be about 20 ms^{-1}. This c_e is used only to create the new dependent variables q and r from u and Z and later to reverse the variable transform.

iii) Transform the Fourier coefficients for each wave mode back into physical space.

The projected n=0, 1 and 2 components will be referred to as WMRG, R1 and R2 waves, respectively. Note that although the winds are broad-band filtered before projection (for each k and n) the fields obtained by the inverse transform capture variation in wave component amplitude with longitude because the range in zonal wavenumber is broad.

iv) Regressing waves onto AEW vorticity centres

To investigate the relationship between equatorial waves and AEWs, linear regression techniques similar to those developed in Yang et al. (2007a, b) are used to regress the horizontal winds of the westward-moving equatorial waves onto vorticity centres tracked at

245 600 hPa across West Africa and the tropical North Atlantic. The regression is based on
246 considering the horizontal fields in a frame where the longitude coordinate is expressed
247 relative to the position of each positive vorticity centre tracked through a region. More
248 specifically, in the regression the independent variable is the value of the tracked vorticity at
249 the location of the maximum falling anywhere within a specified region (e.g., 7.5°W-7.5°E
250 and 5°N-15°N as shown in Fig.2a). The horizontal wind fields (westward-filtered
251 components or the projected equatorial waves) are the dependent variables. The wind fields at
252 each latitude and at each level are regressed onto the positive vorticity centres in a given
253 longitude sector. The regression yields a separate regression equation for each grid point (in
254 the feature-relative frame). The linear dependence of the wind fields can then be mapped by
255 applying the regression equation for each grid point. The regression can also be performed by
256 applying a lag to the dependent variables (wind fields) relative to the independent variable
257 (central vorticity) to investigate the time evolution of waves and their zonal propagation. The
258 regression is performed over all 32 June-September (JJAS) seasons concatenated to obtain the
259 climatology of the wave behaviour in Section 5. It is also performed over 6 strong and 6
260 weak AEW seasons for strong and weak AEW cases, to examine their differences in Section
261 6. The student T-test is used to test the statistical significance for regression coefficients and
262 difference fields between strong and weak AEW years. The significance level of 95% is used
263 in all relevant figures.

264 3. **Climatology of AEWs and equatorial wave variability**

265 Figures 2 a, b show the geographic distribution of frequency (occurrence) and amplitude
266 of positive vorticity centres tracked at 600 hPa, passing through 35°E-10°W and 5°N-20°N in
267 JJAS 1979-2010. It is seen the density is further equatorward over the African continent than
268 across the Atlantic. The low latitude range of occurrence of AEWs provides a potential link
269 between AEWs and westward-moving equatorially trapped waves. The vorticity centres that

propagate to the extratropics with stronger amplitude (Fig.2b) are recurving tropical storms, however, their occurrence frequency is much lower. The area where AEWs are most prevalent is divided into 5 regions, each spanning 15^{o} longitude and 10^{o} latitude, as indicated by the boxes in Fig.2a. They will be used in Sections 5 and 6 for the regression onto vorticity centres passing through each region.

Analysis of the AEW tracks indicates that there is a clear interannual variability both in the frequency and intensity of the vorticity centres of AEWs. Figure 2c shows the time series of amplitude anomaly of vorticity centres averaged over the 5 regions, where six strong and six weak AEW years are identified according to the amplitude being stronger or weaker than one standard deviation. The six years with strongest AEWs are labelled, and the six with weakest AEWs, and these are used to create composites in Section 6.

To examine the overall variability of tropical disturbances over the North African and Atlantic sector (75^{o}W-45^{o}E) in JJAS, space–time power spectra (Hayashi 1982) of meridional winds are calculated. This is done at each latitude and then averaged over 5-18^{o}N. The zonal and temporal Fourier transforms are performed on data from a limited 120^{o} zonal sector and 122 day time windows. Prior to applying Fast Fourier transforms, the zonal average in the 120^{o} sector and time mean over the 122 days are removed and the values are tapered to zero at each end of the zonal sector and time window. The minimum zonal wavenumber that can be determined from data in a 120^{o} sector is k=3 (and spectral coefficients are obtained only for its harmonics k=3, 6, 9, …). Figure 3 shows power spectra of v at 200 hPa and 700 hPa in the 75^{o}W-45^{o}E sector, averaged for all 32 JJAS seasons in 1979-2010. It can be seen that at both pressure levels, the westward-moving (indicated by k<0) power dominates. The strongest power at 700 hPa is clearly coincident with that of typical AEWs with k≈9-15 and period ≈3-6 days. On the other hand, the strongest power at 200 hPa shows smaller wavenumbers and

longer periods than those of AEWs. The box indicates the broad filter domain which is used in this study (see Section 2c).

Figure 4 shows the geographic distribution of variance in westward-moving disturbances and equatorial waves. Longitude-height cross sections depict the standard deviations (SD, daily departure from monthly mean) in meridional wind for westward-filtered components at 12°N, 0°N and 12°S (upper three rows) averaged over 32 JJAS seasons. The projection of meridional wind on to the WMRG wave component is shown at the equator (fourth row). Note that for WMRG waves, because their horizontal structures are untilted, the standard-deviation structure shown is independent of the latitude chosen and only the amplitude changes. As expected, at 12°N where AEWs are prevalent, there is a SD (v) maximum in the lower troposphere over West Africa and the East Atlantic (40°W-30°E). It is clear that this low level feature also occurs for SD (v) at 0°N and for the WMRG wave. It is interesting that in the upper troposphere there is also a maximum SD (v) in the same longitude sector both in the SH (Fig. 4c) and on the equator (Fig. 4b), but not in the NH (Fig.4a). The upper tropospheric maximum also appears for WMRG waves in the sector. The link between wave activity in the SH and AEWs over West Africa will be explored in Section 6.

4 Case study of AEWs in 1995 and relation to tropical cyclogenesis

To examine the connection between AEW vorticity centres and propagating WMRG waves, the 1995 season is investigated in detail including a particular tropical storm that occurred in this season. The 1995 summer was a highly active Atlantic hurricane season that produced 21 tropical cyclones, 19 named storms, as well as 11 hurricanes including 5 major hurricanes. Figure 5a shows the Hovmöller plot of the 600 hPa vorticity tracks passing through 35°E-10°W in JJAS 1995, with vorticity centres in 5°N-20°N indicated by circles. Colours indicate intensity and those leaving the tropics indicated by grey circles. It shows that the amplitude of vorticity tracks in the Atlantic region is generally stronger than that over the

African continent. Figure 5b shows the corresponding Hovmöller plot for the meridional wind of the WMRG waves at 700 hPa, with the vorticity tracks superimposed. It is striking that the westward phase speed of the WMRG waves varies little and is faster than the westward motion of the majority of vorticity centres. Furthermore, there are five periods where there is a distinct eastwards group velocity of WMRG waves over the Atlantic to about 10°E. A particularly marked episode begins in mid-July from the western Atlantic. This group behavior is predicted by equatorial wave theory for WMRG waves (explored further in Section 6) and is evidence that the WMRG structures identified by the projection technique are exhibiting mode-like behavior that is independent of the vorticity centres within the AEWs.

As a case study, the development of a Category 4 hurricane, named 'Felix' is examined (indicated by 'F' in Fig.5). It was reported that on the 6 August, an AEW vorticity centre crossed the west coast of Africa and quickly developed into tropical storm 'Felix' on the 8 August, and then became a Category 4 hurricane on the 12 August. The vorticity track in the first half of August, shown in Fig.5a, demonstrates this event. Figure 6a shows the vorticity centres and westward-filtered horizontal winds at 700 hPa during the 4-9 August. On the 4 August, there is a positive vorticity centre over West Africa, indicated by 'A'. This moves westward and intensifies over the Atlantic, indicating the development of tropical storm 'Felix'. The development of 'A' is associated with strong cross-equatorial flow which propagates westwards with the centre 'A' and projects strongly onto a WMRG wave structure (Fig.6b). On the 4 August 'A' begins in the trough (positive vorticity maximum) of the WMRG wave. Over the 5-7 August, the WMRG wave moves faster to the west, until 'A' is in phase with the strong northward cross-equatorial flow associated with the WMRG wave. On the 8 August, the WMRG wave weakens in the west but intensifies in the east due to its eastward group velocity (wave packet moving eastward). A new vorticity centre, 'B', intensifies in the convergent region just west of the strongest lower tropospheric cross-

equatorial flow of the WMRG wave. It is noted that in this case study, the WMRG has a zonal wavelength of about 60° (k=6, ~6700km), longer than that of the AEW wavelength of 40° (k=9) estimated by the separation of centres 'A' and 'B'.

Figure 7 shows that in the early stages of intensification, 5-7 August, 'A' is also connected to cross-equatorial meridional wind in the upper troposphere (Fig.7a) which again projects strongly onto the WMRG wave (Fig.7b). The cross-equatorial flow has opposite sign to that at 700 hPa, with maximum divergence immediately to the east of 'A' during the 5-7 August. Upper level divergence is in a suitable position for the development of the low level positive vorticity centre by vorticity stretching (as will be shown in Section 6) and it is hypothesized that the WMRG wave may play an important role in the intensification of the vorticity centre and its development into tropical storm category. On 8 August vorticity centre 'B' appears where the meridional wind is weak in the upper troposphere and 'B' does not intensify into a strong storm. It is also noted that on 9 August another vorticity centre 'C' grows to the east of 'B' and in this case intensifies beneath the upper level divergence of the WMRG wave, just as centre 'A' did.

Another interesting feature to note is that in Fig.7a there is a Rossby wave train in the SH, indicated by the pattern of cyclonic and anticyclonic circulations centred near 12°S with a zonal wavenumber of about 5. This pattern moves westward in step with the large scale cross-equatorial flow of the WMRG structure. The importance of SH equivalent barotropic Rossby waves (hereafter RWs) is explored in Section 6.

The case study indicates that WMRG waves are involved in the development of tropical storm 'Felix'. Although the WMRG wave has a much longer wavelength than the separation of centres 'A' and 'B', and moves faster to the west, these vorticity centres amplify when the WMRG wave is in a particular phase with the cross-equatorial flow maximum just to the east of the vorticity centre at the AEJ level.

It should be pointed out that although *u* and *v* are independently projected onto each wave mode without supposing a theoretical relationship between them, the projected (*u*, *v*) for the *n*=0 waves (Figs.6b, 7b) show coherent WMRG wave structures over the whole wave phase. This indicates the robustness in the methodology of identifying equatorial wave modes through projection.

5 Average wave structures associated with AEWs calculated by regression onto vorticity centres

To examine the climatology of wave structures associated with AEWs and to explore whether the conclusions from the 1995 case study are representative of the general situation, the regression technique described in Section 2c is used to regress westward-filtered fields and the WMRG wave wind component onto the vorticity value at the tracked centres within AEWs. The regression is performed using data from the five longitudinal sectors (shown in Fig.2a) for all 32 JJAS seasons spanned by ERA-Interim.

a. Horizontal structures

Figures 8 show the horizontal winds for the 700 hPa westward-filtered winds, and the WMRG wave component at 700 hPa and 200 hPa, regressed onto AEW positive vorticity centres in the region spanning 15^{o} longitude centred at 0^{o}E (see Fig.2a). The regression is calculated with a time lag of -1, 0 and +1 days between the regressed field and vorticity centre amplitude. The corresponding vorticity centres (red circles) are obtained by a self-regression of the centres as described in Section 2c. It is clear that coherent wave structures appear either side of the vorticity centres. The westward-filtered component (Fig.8a) shows a coherent wave train with the negative vorticity centre to the west being stronger at lag -1 and the negative vorticity centre to the east being stronger at lag +1. This is consistent with an eastward group velocity. The WMRG waves (Fig.8b and 8c) propagate faster to the west than

393 the vorticity centres (as seen in the case study). In the lower troposphere, the vorticity centre
394 is located in the WMRG wave trough on day -1 but the vorticity centre is more in phase with
395 the southerly wind of the WMRG wave by day +1. Since the AEW is off equatorial, the
396 positive vorticity centre is located within a region of convergence of the low level northward
397 flow in the WMRG wave. Furthermore, the WMRG negative vorticity centre grows on the
398 eastern flank, as in the full meridional wind, indicating that the observed eastward group
399 velocity within the AEW is explained by the behaviour of the WMRG wave component.
400 Regression fields in the lower troposphere for the other 4 regions show similar structures and
401 phase relationships.

402 In the upper troposphere, the WMRG wave (Fig.8c) has its maximum southward wind in
403 phase with the positive vorticity centre at day-1. The WMRG wave propagates faster to the
404 west than the vorticity centre at this level too. Nevertheless, the regression shows that
405 vorticity centres in AEWs intensify underneath divergence in the upper tropospheric
406 southward flow of the WMRG wave. Note also the westward displacement between the low
407 level convergence (immediately east of the vorticity centre) and upper level divergence (west
408 of the centre) which is examined in the next section. The climatology of regressed horizontal
409 structures of WMRG waves and their relationship with AEWs are entirely consistent with
410 those shown in the case study.

411 *b. Vertical structure of the distinct wave types*

412 The regression of fields onto the value of vorticity at the AEW vorticity centres can be
413 used to extract the vertical structure and tilt associated with the equatorial wave components
414 because the regression is calculated on each pressure level independently as a function of
415 longitude relative to the vorticity centres tracked at 600 hPa (see Section 2(c)iv). Figure 9a
416 shows the longitude-pressure cross-section of the meridional wind (broad-band filtered to
417 isolate the westward moving component) at 12ºN regressed onto the vorticity centres in all 5

418 longitudinal sectors (shown by rectangles in Fig.2a). The meridional wind is further
419 partitioned by projection onto the horizontal structures of the WMRG, R1 and R2 equatorial
420 waves at each level. As described in Section 2b, the equatorial waves form a relevant choice
421 of orthogonal basis functions. The sum of the projections onto R1 and R2 captures most of the
422 structure associated with the vorticity in the AEW itself. It is a convenient way to separate
423 equatorial Rossby wave motion from other components, even though it is not expected that
424 the R1 and R2 components evolve as the corresponding modes would on a resting background
425 state.

426 It is seen that all the wave components increase in amplitude towards the west, being
427 stronger over the East Atlantic than over Africa. Over the ocean (30°W) the tilt of the wave
428 components is weak. The equatorial Rossby wave component is deep, resembling an
429 equivalent barotropic structure. However, the WMRG wave has a clear zero node at about 300
430 hPa where the structure changes sign. This is consistent with the first baroclinic vertical
431 structure that arises in the calculation of normal modes by separation of variables on a resting
432 basic state.

433 However, over West Africa, the equatorial Rossby wave component (Fig.9b) tilts
434 eastward with height (upshear) below theAEJ, at about 600 hPa, and westwards above it
435 which is a necessary configuration for baroclinic wave growth (Thorncroft and Blackburn,
436 1999; Berry and Thorncroft 2005; Cornforth *et al.* 2017). Note that in the full *v* (westward
437 filtered) the tilt below the AEJ is not so apparent, although the westward tilt above the AEJ is
438 clear, which indicates that the projection onto equatorial Rossby wave components does serve
439 to isolate the tilt and connection with the baroclinic growth mechanism (through counter-
440 propagating Rossby waves).

441 The WMRG waves (Fig. 9c) also tilt eastwards below the AEJ and westwards above it.
442 However, the signature of the first baroclinic structure is retained with winds in the upper

443 troposphere having opposite sign to those below, in addition to the westwards tilt above the
444 AEJ. However, the zero node varies in altitude from 300 hPa at 30°W to 400 hPa at 15°E. It
445 is interesting that the WMRG wave structures in the upper troposphere (above the zero node)
446 also exhibit slightly longer wavelengths than in the lower troposphere (quantified in the next
447 section). For *v* at 12°S (Fig.9d), a significant wave signal is found only in the upper
448 troposphere. It is interesting that its pattern is very similar in wavelength and phase to that of
449 the upper tropospheric WMRG waves, suggesting a connection between the WMRG and SH
450 upper tropospheric RWs (examined in Section 6). The lack of coherent signal in the lower
451 troposphere shows that the motions in the SH at this level are uncorrelated with AEWs across
452 West Africa. Therefore the signature seen in the WMRG projection in the lower troposphere is
453 dominated by the NH.

454 *c. Zonal propagation characteristics*

455 The zonal propagation characteristics of waves identified in the meridional wind are
456 quantified in the NH (at 12°N), the SH (at 12°S) and for the WMRG structure (at the equator).
457 Three propagation parameters, the zonal wavenumber (*k*), period (*p*) and phase speed (*c*), are
458 obtained from the regression fields as a function of longitudinal sector and time lag (fields
459 similar to Fig.11e). The zonal phase speed *c* is calculated from this regressed field using the
460 Radon transform method (Radon 1917; Yang et al.2007b). The range of *k* and *p* characteristic
461 of the variability in each wave component is estimated from longitude-lag diagrams.

462 Table 1 shows these propagation parameters for the following fields regressed onto the
463 vorticity value at the tracked AEW centres in the region centred at 0°E: *v* (12°N, 700 hPa), *v*
464 (12°S, 200 hPa) and the WMRG equatorial *v* at 700 hPa and 200 hPa. The westward-filtered
465 *v* (12°N, 700 hPa) is dominated by AEWs and therefore has a characteristic phase speed *c* (9.1
466 m s^{-1}) which is close to the average zonal speed of the tracked vorticity centres (8.4 m s^{-1}).
467 The characteristic zonal wavenumber is 12-13 and the period is 3-4 days. Interestingly, the

period *p* is quite similar for the AEWs, WMRG component and the upper tropospheric wave activity in the SH. The period is found to be slightly longer in the upper troposphere (4-5 days) than lower troposphere (3-4 days). However, since WMRG waves have *k* of 11-12 in the lower troposphere and *k* of 8-9 in the upper troposphere, they have quite similar phase speed *c* (11 and 11.9 m s^{-1}). The difference in zonal wavelength for WMRG waves in the upper and lower troposphere has already been noted from Fig.9c.

The AEW at 700 hPa has a wavelength longer than early studies on AEWs which only used low level meridional wind (e.g., Burpee 1974) or relative vorticity for a limited period (*k=14-19*), but slightly shorter than some later studies (*k=8-13*), e.g., Kiladis et al (2005), where AEW structures were obtained by statistical regression of winds onto westward-filtered OLR (Outgoing Longwave Radiation). Our study shows that the WMRG waves over West Africa have a longer wavelength, particularly in the upper troposphere, and move at similar westward phase speed to AEWs (although faster). Therefore, we deduce that the longer wavelength derived statistically in those studies using OLR is representative of the upper tropospheric WMRG wave component, rather than the vorticity wave on the AEJ.

The westward-filtered *v* at 12^{o}S, which is a signature of SH RWs in the upper troposphere, has the same period as the WMRG waves (4-5 days) and slightly smaller wavenumber *k* (7-8) and therefore on average slightly faster westward phase speed *c* (12.7 m s^{-1}). The mechanism connecting these SH upper tropospheric Rossby waves and WMRG waves is investigated in Section 6d.

6. Years with strong and weak AEW activity and evidence for a major role of Rossby waves propagating from the Southern Hemisphere

The strong inter-annual variability of AEW occurrence has already been discussed in the introduction and Fig. 2c shows the marked variability in average AEW intensity between years. In this section, dynamical mechanisms that might explain the inter-annual variability

493 are sought. In Section 6a, the wave activity throughout the tropics between 75°W and 45°E is
494 characterised for 6 years with the strongest AEW strength and the 6 weakest (labelled in Fig.
495 2c). In Section 6b, mechanisms for amplification of AEW vorticity centres by WMRG waves
496 are explored. In section 6c, it is shown that the differences in seasonal-mean zonal flow
497 between the years with strongest and weakest AEW activity are much larger in the upper
498 troposphere than lower troposphere, extending the findings of Nicholson (2009) who
499 examined a single strong and weak AEW year. Then in Section 6d, Doppler shifting of
500 WMRG waves by basic zonal flows is shown. Finally in Sections 6e-g, the theory for the
501 propagation of RWs and equatorial WMRG waves is used to relate the marked differences in
502 wave activity to the time-mean flow in each season, and a diagnosis of the connection
503 between WMRG waves and SH RWs is present. Dynamical explanations are explored that
504 link enhanced AEW activity to enhanced activity of WMRG waves and RWs propagating
505 from the SH into the tropical wave guide.

506 *a. Differences in tropical wave activity between years with strong and weak AEW activity*

507 Figure10 shows a longitude-height cross section of the standard deviation of
508 meridional wind (SD(v)) for westward-filtered disturbances at 12^{o}N, 0^{o}N and 12^{o}S and the
509 WMRG wave structures, for the six strongest (left column), six weakest (middle column)
510 AEW years and the difference between them (right column). As in the climatology (Fig.4), for
511 both strong and weak AEW years, the SD(v) at 12^{o}N in the lower troposphere shows a local
512 maximum over West Africa and the East Atlantic where AEWs are prevalent. This low level
513 maximum also appears to a lesser extent for SD(v) at 0^{o}N and for the WMRG wave. As
514 expected, at 12°N and the equator the lower tropospheric activity is significantly stronger for
515 the strong AEW years than in the weak years (significance level >95% from a student-T test).
516 However, the WMRG waves shows that they are also significantly enhanced in the upper
517 troposphere at the longitudes with lower tropospheric activity. The WMRG component shows

two distinct maxima in altitude in strong AEW years indicating that the lower and upper tropospheric variability maybe distinct (they have already been shown to have distinct wavenumbers).

There is also an upper-tropospheric maximum in SD(v) in the range 75°W-10°W for westward-filtered disturbances at 12°S and on the equator, as well as for WMRG waves, which is significantly stronger in strong AEW years (Figs. 10c and 10d). The reasons for this are explored in Section 6c.

b. Mechanisms for amplification of AEW vorticity centres by WMRG waves

The close connection between increased WMRG wave activity and AEW activity suggests the importance of the WMRG wave for the development of the AEWs and interannual variability. The consistent phase relationship between the AEW vorticity centres and the WMRG wave structure in the lower and upper troposphere has already been shown in Fig.8 through the regression analysis. Here, Figs.11a, b show the 200hPa horizontal winds for westward-filtered disturbances and the WMRG structures, both regressed onto the vorticity centres passing through the region centred at 0^{o}E. The results are shown for the entire climatology, strong and weak AEW years. It is clear that in all cases there are strong large-scale circulations extending across the equator, with the cross-equatorial motion dominated by the WMRG structure and southward cross-equatorial flow at the longitude of the vorticity centre. The winds are in the correct phase to amplify the vorticity centres through vortex stretching. Cross-equatorial flows are weaker for climatology and weak AEW years.

The hypothesised mechanism of vorticity stretching by the WMRG waves is explored in Fig. 11c which shows the longitude-height cross-section of vorticity stretching - f^*D averaged over 5^{o}N-18^{o}N for the winds projected onto WMRG waves. f^* denotes the basic state absolute vorticity ($f - dU/dy$) and D is the horizontal divergence in the WMRG wave. The diagnostic reveals that the term is positive at the location of the AEW vorticity centre (0^o

543 on the shifted longitude axis) and to its east, implying that the WMRG structure acts to
544 intensify the vorticity centre and to hinder its propagation towards the west. In weak AEW
545 years the vorticity stretching is weaker, about 60% of that for strong years at 600 hPa. The
546 peak magnitude of vorticity stretching at 600hPa in strong AEW years is about $4*10^{-11}$ s^{-2},
547 which corresponds to a vorticity tendency of $0.13*f$ per day, which is strong relative to the
548 observed rate of amplification (see e.g., Fig.5).

549 To examine the time evolution of the WMRG wave and its connection to the AEW in the
550 lower troposphere, Fig. 11d shows a lag time-height diagram of the WMRG waves, where the
551 independent variable is the maximum vorticity in the AEW trough and the dependent variable
552 (meridional wind of the WMRG component) is regressed with varying time lags such that
553 "day 0" corresponds to the time of maximum vorticity. This indicates that in strong AEW
554 years the upper tropospheric WMRG waves are much more prevalent than in the climatology
555 and the weak AEW years, and this is also true in the lower troposphere.

556 Fig. 11e presents the longitude-time diagram for WMRG waves at 200 hPa regressed onto
557 the vorticity of the AEW centres. The WMRG northerly wind is in phase with the vorticity
558 centres at the beginning of the vorticity track in years of strong and weak AEWs, consistent
559 with vortex stretching as a mechanism to intensify the vorticity. However, an important
560 feature is that well before the vorticity track starts, there are WMRG wave trains with
561 eastward group velocity propagating into the region from the Atlantic, especially in strong
562 AEW years. This provides evidence that the WMRG waves indeed play an important role in
563 the amplification of the AEWs, rather than the WMRG waves being an inherent part of the
564 AEW structure. The difference in westward phase speed between the WMRG waves and
565 AEWs is also clear. It is also interesting to note that in strong AEW years at around 0^o
566 longitude the MRG wave packet has near zero group velocity, and in negative lag days to the
567 east of 0^o there is also a weak wave train with westward group speed. As will be shown

568 below, this variation in the WMRG group velocity is consistent with the change in the
569 dispersion relation of the WMRG wave due to the change in the basic zonal winds, and near
570 zero group velocity around 0^{o} longitude suggests the wave energy accumulation there.
571 There is a strong relationship between developing AEW vorticity centres in the NH lower
572 troposphere and WMRG waves. Figures 8 and 9 show that in the lower troposphere, there is
573 northward cross-equatorial flow and a maximum in convergence just to the east of the
574 vorticity centres. In the upper troposphere, there is a maximum in divergence as part of
575 WMRG structures just to the west of the vorticity centre, and associated southwards flow
576 across the equator. This phase relationship is similar to the one Besson and Lemaitre (2014)
577 identified with intense and long-lived mesoscale convective systems (MCSs) embedded
578 within AEWs close to the positive vorticity centre. The MCS occurs where there is ascent
579 precisely between upper level divergence to the west and low level convergence to the east
580 (see their Fig.5). Besson and Lemaitre (2014) describe the upper tropospheric feature as a
581 "TEJ streak". Deep convection and latent heat release occurs within the MCS and this would
582 act as a positive feedback onto the ascent associated with the tilted WMRG structure. The
583 ascent shown in their work is in the correct phase to amplify the low level positive vorticity
584 centre by vortex stretching.
585 The average location of convection relative to vorticity centres is shown in Fig.12.
586 Outgoing Longwave Radiation (OLR) and westward-filtered horizontal winds in the upper
587 and lower troposphere are regressed onto the AEW vorticity centres in the two longitudinal
588 sectors centred at 15^{o}W and 0^{o}E (for strong AEW years). It is seen that intensified convection
589 (negative OLR anomaly) is collocated with the positive vorticity centres and on their eastern
590 flank where the lower tropospheric cross-equatorial flow from the SH is strongest, but also
591 where the vortex stretching by the WMRG component is strongest. It illustrates the
592 connection between the AEW vorticity at 700 hPa, ascent, OLR (as a proxy for deep

593 convection), upper level divergence and cross equatorial motion as part of a WMRG wave.
594 The latent heat release within convection is in the correct phase to amplify the vertical motion
595 and AEW vorticity. The large meridional extent of winds associated with the OLR in the
596 AEWs is consistent with that shown in Kiladis et al. (2006). They suggest that the convection
597 associated with AEWs is initiated by dynamical forcing which leads to vertical motion at low
598 levels and couples the AEW to deep convection.

599 Note that this synoptic scale explanation for the link between seasons with stronger
600 vorticity centres in AEWs and enhanced WMRG activity differs markedly from the argument
601 made by Nicholson (2009) that enhanced season-average precipitation in years of strong
602 AEW activity was a result of greater time-mean ascent in the rain-belt and a stronger TEJ.
603 The stronger precipitation must be associated with stronger ascent (through the time-mean
604 thermodynamic budget typical of the tropics) and together they are related to a stronger
605 meridional circulation, southward flow in the upper troposphere and a stronger TEJ to the
606 south of the rain belt. This is a diagnostic relationship, not a causal one. In the following
607 section, the differences in seasonal-mean zonal flow between years with strong and weak
608 AEWs will be calculated and then in Sections 6d and 6e they will be used as input to diagnose
609 the Doppler-shifting of WMRG waves and to wave propagation theory to explain why wave
610 activity is greater when the TEJ is strong.

611 *c. Difference in basic zonal flow between years of strong and weak AEW activity*

612 Figure 13 shows seasonal-mean zonal winds in the upper and lower troposphere, averaged
613 for the 6 strongest and 6 weakest AEW years and the difference between them. In the lower
614 troposphere, the difference in the zonal winds is small with the easterly flow being slightly
615 weaker over 0°-15°N in strong AEW years. Note that on a meandering jet, if the meanders (or
616 waves) have greater amplitude then the zonal average of the flow has a weaker magnitude,

617 even if the wind speed along the curvy jet core is the same. This effect may explain the slight
618 reduction in easterly flow in years of strong AEWs.
619 The zonal flow difference in the upper troposphere is far greater and dominated by
620 easterly anomalies. The time-average zonal wind is anomalously easterly in strong AEW
621 years in the equatorial region and the SH tropics across the Atlantic and southern Africa. The
622 equatorial easterly flow is stronger and the westerly flow in the SH (south of 5-10°S) is
623 weaker. This is consistent with the finding of Nicholson (2009). Now the ramifications of
624 seasonal-mean zonal flow differences for the propagation and activity of RWs and equatorial
625 WMRG waves is investigated. Enhanced activity in WMRG waves above West Africa is
626 expected to enhance AEW activity through the vortex stretching mechanism described in the
627 last section.

628 *d. Doppler shift of WMRG waves by stronger easterlies*

629 To examine the influence of extratropical RWs on tropical WMRG waves, it is
630 instructive to analyse the properties of equatorial wave dispersion, RW dispersion on the
631 sphere and the conditions for the reflection or absorption of Rossby wave rays.
632 Figure 14a shows the observed time-mean zonal-mean flow profile $U(\varphi)$ averaged
633 across the 75°W- 45°E sector in the upper troposphere for strong (black line) and weak (grey
634 line) AEW years. It is seen that the easterly flow in the tropics is stronger and broader in
635 strong AEW years. The curvature of the broader jet is weaker and therefore the effective β is
636 closer to the value of planetary vorticity gradient. Figure14b shows two sets of equatorial
637 wave dispersion curves corresponding to two Doppler shifts by U_0 values (average zonal
638 wind over the longitude sector and latitudes between $+2y_0$ and $-2y_0$) in strong and weak
639 AEW years, respectively. The planetary vorticity gradient β_0 is used for the dispersion
640 relations (without considering the relative vorticity of the background flow) to be consistent
641 with the assumptions in the basic equatorial wave theory (Matsuno, 1966). Since U_0 in weak

642 AEW years is small (-1.9 ms^{-1}), the corresponding dispersion curves (grey) are not far from
643 the familiar results for a resting atmosphere. In strong AEW years there is stronger easterly
644 flow (- 5.8 ms^{-1}) and the eastward-moving waves (Kelvin waves and EMRG waves) are
645 Doppler shifted to lower frequency. The westward-moving WMRG and R1 waves are shifted
646 to higher frequency, especially for larger *k*. It is important to note that due to the Doppler
647 shifting, the frequency for WMRG curves becomes very flat across a wide range of *k*. As a
648 result, the period of WMRG waves is almost uniform (3-4 days) in strong AEW years which
649 is comparable to the period of AEWs. The period range predicted by theory is close to that of
650 the observed WMRG waves (Table 1) and with the typical period of AEWs.
651 In the easterly environment, the group velocity of WMRG waves ($\partial\omega/\partial k$) is near zero
652 (solid black curve in Fig.13b). The eastward group velocity is greater in regions with weaker
653 easterlies for small *k* (solid grey curve). This implies that the eastward-group velocity of
654 WMRG waves must be stronger over South America and the western Atlantic where easterly
655 wind is weaker, while over the African continent the group velocity will become close to zero
656 due to the stronger easterlies. Therefore wave energy accumulation must occur over West
657 Africa (Hoskins and Yang 2016). This change in the WMRG group velocity is entirely
658 consistent with that shown in Fig.11e. Ray tracing for WMRG waves with a period of -4 days,
659 following the one-dimensional calculation of Hoskins and Yang (2016), indeed shows that
660 there is energy accumulation over West Africa where the group velocity approaches zero (not
661 shown here). This is consistent with the local maximum in SD(v) associated with WMRG
662 waves in the upper troposphere over the West African coast (Fig10 d). Note that Diaz and
663 Aiyyer (2013) applied lag regression analysis to re-analysis data to deduce that AEWs exhibit
664 eastward group velocity to the west of 0°E at all levels over the Atlantic and west coast of
665 North Africa. Although they examined the energetics of wave propagation, they did not make
666 the connection with WMRG waves. The eastward-group velocity of the WMRG waves may

Explain the eastward-group velocity observed in their statistical analysis over the west side of West Africa since the two components are difficult to disentangle without the projection step.

e. Rossby wave propagation into the tropical wave guide

Free Rossby wave propagation across the extratropics and in the upper troposphere in the tropics is now analysed using the barotropic vorticity equation. Following Hoskins and Karoly (1981), Hoskins and Ambrizzi (1993) and others have shown that the Rossby ray paths calculated using this reduced dynamics can explain many prominent equivalent-barotropic stationary wave patterns in the atmosphere. Furthermore, Hoskins and Karoly (1981) have shown that the vorticity equation for disturbances on the sphere viewed from the Mercator projection is formally similar to the equation on a Cartesian β-plane which simplifies the mathematical analysis. The dispersion relation can be written:

$$\omega = U_M k - \frac{\beta_M k}{k^2+l^2} \quad (7)$$

where l is the meridional wavenumber, $U_M = U/\cos\varphi$, is the zonal angular velocity of the background flow, $\beta_M = \frac{2\Omega cos^2\varphi}{a} - \frac{d}{dy}\frac{1}{cos^2\varphi}\frac{d}{dy}(cos^2\varphi U_M)$ is the relevant meridional absolute vorticity gradient modified by the curvature of the basic zonal wind. In this expression, a denotes the Earth's radius, φ is latitude and $y=a\varphi$. From now on the M-subscript will be dropped but it is implicitly understood that the analysis applies to the Mercator projection of a domain spanning the tropics and subtropics. It should be noted that k in all equations is the dimensional zonal wavenumber to be distinguished from that used in the figures where it is the non-dimensional value $\tilde{k} = ak$. In the Rossby wave analysis, following previous authors, the convention will be that the zonal wavenumber is positive definite and westward propagation will be associated with $\omega<0$ (in contrast to the convention used for equatorial waves where the wavenumber changes sign).

690 Hoskins and Karoly (1981) also showed that following RW rays, ω and k are constants
691 (when U and β are independent of x and t) and l varies such that the dispersion relation (Eq.7)
692 is satisfied**.** Therefore we can consider ω as a given parameter and seek conditions on k for the
693 propagation of rays.
694 As discussed in Hoskins and Ambrizzi (1993), the theory can be successfully applied to a
695 longitudinally varying basic flow, assuming that the variation of U_M and β_M with longitude is
696 on a longer scale than the wavelength of interest. Yang and Hoskins (1996) extended the
697 theory to the propagation of Rossby waves of positive and negative frequency. Following ray
698 paths through a slowly varying medium, two behaviours can occur:
699 i) The ray approaches a turning latitude when it turns into the zonal direction and $l \rightarrow 0$
700 and the ray is reflected back towards the equator. When l=0, Eq.(7) reduces to the quadratic
701 equation $Uk^2 - \omega k - \beta = 0$, which has two roots:

$$k_{1,2} = [\omega \mp (\omega^2 + 4\beta U)^{1/2}]/(2U) \qquad (8)$$

703 ii) The ray approaches a critical line where $c=\omega/k=U$. As it does so, the meridional scale
704 must shrink, the meridional group velocity decreases and the critical zonal wavenumber k_c=
705 ω/U is only achieved where l asymptotically approaches infinity. Yang and Hoskins (1996)
706 outline the conditions for nonstationary RW propagation with the detailed solution and
707 schematic picture for allowable k in different basic states. It is shown that westward-moving
708 RWs can exist on both westerlies and easterlies. The relevant case here is $\beta>0$ and $\omega<0$
709 (westward propagation) with different U conditions:

710 - westerlies $U > 0$: propagation is allowed for any $k < k_2$ and there is no critical line.
711 - weak easterlies $U_e < U < 0$: propagation for longer wavelengths $k < k_2$ and there is
712 another shorter wavelength band $k_1 < k < k_c$ where propagation is possible. Here the
713 parameter $U_e = -\omega^2/4\beta$.

- strong easterlies $U<U_e$: propagation is allowed for any $k < k_c$ and there are no reflection lines.

Figures 14 c, d show the ranges of k where RW propagation is possible at each latitude using the observed zonal wind profiles in strong and weak AEW years, respectively, for a specified period of -4 days (the negative denoting westward phase speed). The period is chosen based on the observed period of AEWs (Table 1). The permitted zonal wavenumber range for propagation (shading) is bounded at high k by critical line absorption (dotted) within the tropics and reflection (solid) curves outside the tropical wave guide. Very different RW propagation features are seen between the strong and weak AEW years.

In strong AEW years, due to stronger easterly flow in the SH and equatorial belt, there is a broad tropical wave guide between the two hemispheres. Rossby wave rays with $6<k<12$ can only propagate westwards between 5°S and 17°N with the 4-day period. Westward longwaves with $k \leq 5$ can exist with a 4-day period outside the tropical wave guide owing to their stronger westward propagation rate relative to the zonal flow. In contrast for weak AEW years, RWs propagation is not possible between 2 and 8°N with a period of -4 days because $U_e<U<0$ across those latitudes. Only waves with very long wavelengths ($k<2$) are able to propagate through the equatorial region with this period and therefore the hemispheres are disconnected for shorter wavelengths.

f. Phase speed matching between Rossby and WMRG waves

Above analysis shows that stronger easterlies enable RW propagation at zonal wavenumbers and frequencies comparable with AEWs across the tropical belt. However, how does RW activity in the SH subtropics connect with the WMRG wave activity? Consider the influence of the basic state on the WMRG waves. The dispersion relation for the WMRG wave on a uniform flow, U_0, can be derived from Eq. (3) with meridional mode n=0

738 $$c_{MRG} = \frac{\omega_{MRG}}{k} = U_0 + \frac{c_e}{2}\left(1 - \sqrt{1 + \frac{4\beta}{k^2 c_e}}\right), \qquad (9)$$

739 where U_0 represents an average flow over the equatorial region (between $+2y_0$ and $-2y_0$),
740 $\beta_0=2\Omega/a=2.28*10^{-11}$ m^{-1} s^{-1} and c_e =20 m s^{-1} can be deduced from $y_0 = (\frac{c_e}{2\beta})^{1/2}$=6°, the best
741 fit meridional scale to observed wave structures, as mentioned in Section 2b.

742 Figure 14e,f shows the RW phase speed $c_2=\omega/k_2$ (solid) along the reflection line in
743 Figs.14c,d and the WMRG phase speed, $c_{2\text{-MRG}}$, deduced from Eq. (9) at wavenumber $k_2(\varphi)$
744 (dashed). It is remarkable that the two phase speeds are very close across all latitudes,
745 especially for strong AEW years north of 12°S. In the short wavelength limit $\beta/(k_2 c_e)<<1$, the
746 WMRG dispersion relation (Eq.9) reduces to the barotropic RW dispersion relation (Eq.7) for
747 l=0 (at the reflection lines). For longer waves, the matching phase speed is explained by the
748 flatness of the Doppler-shifted WMRG dispersion curve which has a period close to -4 days
749 for zonal wave numbers 4-16 (Fig.14b). The theoretical prediction is consistent with the
750 observed feature that WMRG and disturbances in v at 12°S have a similar phase speeds
751 (Table 1). Since the phase speeds match, sustained interaction between the Rossby and
752 WMRG waves is expected in the shear flow (in a uniform flow the equatorial wave analysis
753 yields normal modes that cannot interact). For example, in the case study Fig.7 shows how the
754 winds associated with a Rossby wave in the SH (centred at about 12°S) are connected with
755 the WMRG wave structure. Figure 10 also shows how SH Rossby wave activity across the
756 Atlantic and South America is much greater during the strong AEW years (Fig. 10c). In
757 contrast, the upper tropospheric disturbances are not enhanced in the NH (Fig. 10a).

758 *g. Mechanism for excitation of WMRG waves by Rossby waves from the SH*

759 The connection between WMRG waves and Rossby waves from the SH is investigated
760 by regressing the full (unfiltered) horizontal winds onto the northerly wind extrema
761 (minimum v) of the WMRG component. For illustration, the region centred at 15°W is chosen

762 (spanning 30^{o} longitudes) because this is where the standard deviation of WMRG waves is
763 greatest (Fig.4). Only the seasonal mean and zonal (70^{o}W-50^{o}E) mean are removed from the
764 winds used in the regression so that no assumptions are made regarding the spatial structure
765 or frequency of the field. Figures 15 a, b show the regression fields at lag day -1 for strong
766 and weak AEW years, with negative lag indicating full winds lead the WMRG amplitude in
767 cross-equatorial flow (at shifted longitude 0). It is interesting to see that in strong AEW years,
768 to the southwest of WMRG waves there is a SH extratropical wave train with a zonal wave
769 number about 5 and NW-SE tilt, and the eastern part of the wavetrain is dominated by
770 WMRG wave structures. Such a wave train arching from the SH toward the equatorial region
771 is very similar to that in an earlier observational study (Yang and Hoskins 2016) which
772 reveals that WMRG waves in the upper tropospheric eastern Pacific in winter are forced by
773 SH wave trains arching into the equatorial region. In contrast, this feature is not seen in weak
774 AEW years.
775 The NW-SE tilt of the eddy structure implies two points about the relation between
776 WMRG waves and Rossby waves:
777 i) the pattern is consistent with excitation of the WMRG wave by meridional
778 advection of planetary vorticity by the flow associated with SH Rossby waves. For
779 example, consider a thought experiment where there is no WMRG activity and a
780 Rossby wave is focussed on the northern flank of the subtropical jet in the SH.
781 Northward flow to the west of the negative vorticity centre in the wave advects
782 more negative vorticity from the south so that there is an anomalously negative
783 vorticity at that location extending to the equator. A similar argument applies to
784 positive vorticity advection to the east. The net result, as depicted by the schematic
785 (Fig.19) in Hoskins et al (1985) is that a vorticity wave amplifies near the equator
786 with a westward shift of 90° relative to the original wave. Furthermore, although

the WMRG wave can be excited by the Rossby wave by this mechanism, the phase is such that the meridional advection by the WMRG wave acts to decrease the amplitude of the Rossby wave to the south. The interaction therefore has a directional inference. It also implies that the WMRG waves should have a similar wavenumber to the Rossby waves that excite them and if they can propagate with matching phase speeds then the interaction could be sustained.

ii) The tilt implies that the momentum flux [u*v*] is negative which implies that the meridional component of the Rossby wave flux is northward (F_y=-[u*v*]).

The momentum flux of the regressed winds is averaged over two wavelength range of 144° (68°W to 80°E) and shown in Fig.15c, for strong (solid) and weak (dotted) AEW years. In strong AEW years, there is a strong negative [u*v*] in the SH peaking at about 20°S on the equatorward flank of the subtropical westerly jet where there is the strongest meridional shear. This feature is far weaker in years of weak AEW activity, consistent with the untilted wind structure seen in regression (Fig.15b). However, the positive momentum flux on the equator is quite similar in the two cases. Therefore, there is a much stronger convergence of Rossby wave activity from the SH into the tropical wave guide in the strong AEW years.

In addition to the excitation of WMRG waves with similar phase speeds to the SH Rossby waves, the momentum flux convergence will accelerate the tropical easterlies in the upper troposphere (i.e., $\partial[u]/\partial t \sim -[u^*v^*]_y < 0$). However, the magnitude is approximately 5×10^{-7} ms^{-2} which is equivalent to 1.5 m s^{-1} if sustained over 30 days. Therefore, although the Rossby wave convergence into the tropical wave guide gives a positive feedback on the easterly zonal flow (which strengthens the wave guide), the feedback is weak.

7. Conclusions

Dynamical mechanisms influencing the marked inter-annual variability in AEWs were explored by comparing years with the strongest and weakest AEW activity. The biggest differences in the seasonal-mean zonal winds between years of strong and weak AEW activity were found in the upper (rather than lower) troposphere. The Tropical Easterly Jet is stronger in seasons when AEWs are more active, as found by Nicholson (2009). Surprisingly, although the AEWs are examined in the NH lower troposphere, the correlated signal in background wind is strongest in the equatorial and SH upper troposphere. It is also shown that there is enhanced upper tropospheric Rossby wave activity in the SH and WMRG activity in years with the strongest AEWs.

The dynamical connection between African Easterly Waves (AEWs), equatorial westward-moving mixed Rossby-gravity (WMRG) waves and extratropical equivalent barotropic Rossby waves (RWs) from the SH has been investigated using ERA-Interim data for the period 1979-2010. The methodology of Yang et al. (2003), based on projection of broad-band filtered data onto the horizontal structures from equatorial wave theory, is used to identify the equatorial wave components, quantify their variance and identify relationships between them in the development of AEWs. The analysis is conducted on each pressure level independently which enables a characterization of the vertical structure and tilt associated with the wave types. AEW propagation was identified by tracking the positive vorticity centres at the level of the African Easterly Jet (600 hPa).

A case study of the 1995 season was instructive and showed the propagation of the different wave types and the phase relationships between them at times when positive vorticity centres within AEWs intensify. Many of these vorticity centres developed into tropical storms over the Atlantic, some becoming hurricanes. The results were generalized to the entire climatology by using a method whereby all fields were analysed at longitudes relative to AEW vorticity centres and linear regression was used to extract the structures

associated with the vorticity at the tracked centre. The results from the case study period were found to be robust and reflect behavior throughout the re-analysis.

Based on the above observations, mechanisms are deduced for the influence of the seasonal-mean zonal flow on RW propagation into the tropics, the excitation of WMRG waves and their role in the transient intensification of AEWs:

- Stronger easterlies enable a broad tropical waveguide for RWs with the characteristic AEW period of ~4 days. RW dispersion analysis shows that the wavenumber range $5< k <12$ is trapped within the tropical wave guide, while longer waves have strong enough westward propagation to attain the ~4 day period outside the easterly wave guide. For $k=5$, waves are observed to propagate from the SH and converge into the equatorial region (Fig.15). When easterlies are weaker, Rossby wave propagation is not permitted north of the equator with the period ~4 days, closing the connection between hemispheres.
- Stronger easterlies Doppler-shift WMRG waves so that they have a period of about 4 days for a wide range of wavenumbers. In this situation, the tropical wave guide supports Rossby waves with phase speeds that can match Doppler-shifted WMRG waves across the wavenumber range $5<k<12$. This enables sustained interaction of the two waves in the shear flow and excitation of WMRG wave activity through meridional advection of planetary vorticity by SH Rossby wave disturbances as they propagate westwards in step. The dominant wavenumber for WMRG and SH RWs (Table 1) is found to be 7-9 in the upper troposphere with an average phase speed of approximately 12-13 ms^{-1}. Therefore the wave structures that regress onto the AEW vorticity centres (Figs. 8, 9, 11) have slightly shorter wavelengths than the dominant wavenumber flux from the SH subtropics (Fig.15).
- Over South America and the tropical western Atlantic, where upper tropospheric easterlies are weak, the WMRG wave trains have an eastward group velocity and therefore packets move eastwards. However, over Africa where the easterlies are stronger, the effect of

Doppler-shifting the WMRG dispersion relation results in near-zero group velocity and therefore WMRG wave energy must accumulate above West Africa.

- Individual vorticity centres in AEWs amplify when the phase of the WMRG waves are in a particular configuration. The peak amplitude in AEW vorticity occurs when the maximum low level convergence in the WMRG wave (and associated northward flow across the equator) is just to the east of the centre and the maximum upper level divergence (and associated southward flow across the equator) is just to the west of the vorticity centre. Thus the westward tilt of the WMRG component is central to vorticity amplification. In the modal WMRG solution on a resting basic state, the upper level divergence would be associated with upward motion between lower and upper tropospheric layers and compensating horizontal convergence below (both layers with matching horizontal structure as in Fig.1). This mechanism can explain the existence of the strong WMRG activity in the lower troposphere over the East Atlantic and West Africa with a vertical structure similar to a tilted first baroclinic mode. However, in shear flow the wave disturbances are not orthogonal and the vortex stretching associated with the WMRG motion is shown to be in the correct position to amplify the AEW vorticity centre. This occurs even though the WMRG waves (in the upper troposphere) are longer and have faster westward phase speeds. The mismatch in phase speed (see Table 1), but approximate match in frequency, implies a periodic amplification of AEWs associated with WMRG waves at the average timescale of 4 days.
- The lower tropospheric WMRG wave structures advect moisture from the equatorial ocean into West Africa and the OLR signature of deep convection is observed to occur in concert with the AEW vorticity centre and on its eastern flank, precisely where the vortex stretching is found to occur. Latent heat release would act as a positive feedback on the ascent within the wave structure and the amplification of vorticity.

- Finally, the RW activity flux from the SH converges in the tropical wave guide in years of strong AEW activity. This acts as a positive feedback since the flux convergence accelerates the easterly flow, broadening the wave guide and enabling the wave interactions described above. However, this effect was found to be a weak feedback but would contribute to maintenance of stronger easterlies.

It is a surprising finding that the inter-annual variability in AEW activity is more strongly influenced by the background state in the upper troposphere of the SH than NH. The mechanism proposed here is based on the evidence found in terms of the activity in distinct westward propagating wave types identified in re-analyses. Fundamental support for the mechanism is based on the dispersion relations for RWs and WMRG waves and their propagation relative to a smoothly varying background flow (assumed to be represented by the seasonal mean). Therefore the links are non-local and connect the hemispheres. They are mediated by waves with non-zero frequency, as opposed to the more typical teleconnections identified with stationary Rossby waves. An important consequence is that interannual variability of precipitation across West Africa, and longer term climate change, is unlikely to be explained solely by local mechanisms, such as the influence of the land surface.

This study has focused on the influence of background zonal flow on wave propagation characteristics. However, it does not preclude two-way interaction where the TEJ is stronger as a result of greater AEW activity. Also it does not dismiss other processes which are important for the initiation and intensification of AEWs. Greater AEW activity is associated with more deep convection, latent heat release and time-mean ascent in the rain belt across the West Africa. Nicholson (2009) notes this occurs in a year with strong AEW activity and also the equatorward flow from upper level divergence is stronger and so is the TEJ, as would be expected from an enhanced meridional circulation and Coriolis effect turning the southward flow. A positive feedback between enhanced upper tropospheric equatorial easterlies and

AEW activity is plausible. However, there are many other remote influences on the TEJ – for example, the outflow from the Asian summer monsoon convection and the wave activity flux convergence from SH Rossby waves. Therefore, the mechanisms proposed here cannot comprise a closed explanation of AEW interannual variability and it would be interesting to explore in more detail the origins of variability in upper tropospheric zonal flow across the tropical Atlantic, especially in the SH.

The wave theory used in this study is also far from a complete description of wave behaviour in the atmosphere. The equatorial wave theory defining the horizontal structures used for projection of the data does not take into account shear in the zonal flow. This is a limitation, particularly across West Africa where the strong shears associated with the AEJ are essential to the existence ofAEWs. However, the analysis suggests that the observed wave structures do bear some relation to the horizontal structure of the WMRG mode and that vertical shear lends the waves a slight tilt, but does not alter them substantially. This suggests that a more complete theory might be possible where the effects of shear are treated as a perturbation to the structures on uniform flows. Several approaches to this problem have been attempted (Andrews and McIntyre, 1976; Han and Khouider, 2010). Key quantities to predict would be the degree of wave tilt, the structure of vertical motion and its phase relative to the horizontal flow and the role of latent heat release. It has been argued here that the ascent is central to AEW intensification by WMRG packets entering Africa from the Atlantic.

Acknowledgments. GYY acknowledges the long-term support of the National Centre for Atmospheric Science (NCAS). The research was conducted as part of the NERC project (NE/I012419/1). We thank the three reviewers for their very helpful comments which encouraged us to improve the analysis and present evidence for wave interaction mechanisms.

References

Andrews, D. G., and M. E. McIntyre, 1976: Planetary waves in horizontal and vertical shear: Asymptotic theory for equatorial waves in weak shear. *J. Atmos. Sci.*, **33**, 2049–2053.

Agustí-Panareda, A., Beljaars, A., Ahlgrimm, M., Balsamo, G., Bock, O., Forbes, R., Ghelli, A., Guichard, F., Köhler, M., Meynadier, R. and Morcrette, J.-J. (2010), The ECMWF re-analysis for the AMMA observational campaign. Q.J.R. Meteorol. Soc., 136: 1457–1472. doi:10.1002/qj.662

Avila, L. A., and R. J. Pasch, 1992: Atlantic tropical systems of 1991. *Mon. Wea. Rev*., **12**0, 2688–2696.

Avila, L. A., and R. J. Pasch, 1995: Atlantic tropical systems of 1993. *Mon. Wea. Rev*., **123**, 887–896.

Berry, G. J., and C. Thorncroft, 2005: Case study of an intense African easterly wave. Mon. Wea. Rev., 133, 752–766.

Berry, G. J., C. Thorncroft, and T. Hewson, 2007: African easterly waves during 2004—Analysis using objective techniques. Mon. Wea. Rev., 135, 1251–1267.

Besson, L. and Y. Lemaitre, 2014: Mesoscale convective systems in relation to African and Tropical Easterly Jets. *Mon. Wea. Rev.*, **142,** 3224-3242.

Burpee, R. W., 1972: The origin and structure of easterly waves in the lower troposphere of North Africa. *J. Atmos. Sci*., **29**, 77–90.

Burpee, R. W., 1974, Characteristics of North African easterly waves during the summers of 1968 and 1969, *J. Atmos. Sci*., 31, 1556 – 1570.

Burpee, R. W., 1975: Some features of synoptic–scale waves based on a compositing analysis of GATE data. *Mon. Wea. Rev.,* **103,** 921–925.

Carlson, T. N., 1969a: Synoptic histories of three African disturbances that developed into Atlantic hurricanes. *Mon. Wea. Rev., **97,*** 256–276.

Carlson, T. N., 1969b: Some remarks on African disturbances and their progress over the tropical Atlantic. *Mon. Wea. Rev.,* **97,** 716-726.

Cornforth, R. J., B. J. Hoskins, and C. D. Thorncroft, 2009: The impact of moist processes on the African easterly jet–African easterly wave system. Quart. J. Roy. Meteor. Soc., 135, 894–913.

Cornforth, R. J., Mumba, Z., Parker, D. J. *et al.* 2017: Synoptic Systems (Chapter 2) in the *Meteorology of Tropical West Africa: The Forecasters' Handbook*. Editors: Parker, D. J. and Diop-Kane, M., Wiley, 528pp, ISBN: 978-1-118-39130-3.

Crétat, J., E. K. Vizy, and K. H. Cook, 2015: The relationship between African easterly waves and daily rainfall over West Africa: observations and regional climate simulations. *Clim Dyn* , **44**: 385. doi:10.1007/s00382-014-2120-x

Dee D. P., and Coauthors, 2011: The ERA-Interim reanalysis: configuration and performance of the data assimilation system. *Q.J.R. Meteorol. Soc*., **137**: 553–597.

Diaz, M. L., and A. Aiyyer, 2013: Energy dispersion in African easterly waves. *J. Atmos. Sci.*, **70**, 130–145.

Diedhiou, A., S. Janicot, S. Viltard, and H. Laurent, 1999: Easterly wave regimes and associated convection over West Africa and the tropical Atlantic: Results from NCEP/NCAR and ECMWF reanalyses. *Climate Dyn.,* **15,** 795–822.

Duvel, J. P.,1990, Convection over tropical Africa and the Atlantic Ocean during northern summer. II: Modulation by easterly waves, Mon. Weather Rev., 118(9), 1855–1868.

982 Fink, A. H., and A. Reiner, 2003, Spatiotemporal variability of the relation between African
983 easterly waves and West African squall lines in 1998 and 1999. J. Geophys. Res.,
984 108(D11), 4332, doi:10.1029/ 2002JD002816.
985 Frank, N. L., 1970: Atlantic tropical systems of 1969. *Mon. Wea. Rev*., 98,307–314.
986 Gill, A. E., 1980: Some simple solutions for heat induced tropical circulations. *Quart. J. Roy.*
987 *Meteor. Soc.*, **106,** 447–462.
988 ——, 1982: Atmosphere–Ocean Dynamics. Academic Press, 662 pp.
989 Han, Y., and B. Khouider, 2010: Convectively coupled waves in a sheared environment. *J.*
990 *Atmos. Sci.*, **67**, 2913-2942.
991 Hayashi, Y., 1982: Space-time spectral analysis and its applications to atmospheric waves. *J.*
992 *Meteor. Soc. Japan*, **60**, 156–171.
993 Hall, N. M. J., G. N. Kiladis, and C. D. Thorncroft, 2006: Three-dimensional structure and
994 dynamics of African easterly waves. Part II: Dynamical modes. *J. Atmos. Sci.,* **63,**
995 2231–2245.
996 Hopsch SB, Thorncroft CD, Hodges KI, Aiyyer A. 2007. West African storm tracks and their
997 relationship to Atlantic tropical cyclones. J. Climate. 20: 2468–2483.
998 Hoskins, B.J., D. J. Karoly, 1981: The steady linear response of a spherical atmosphere to
999 thermal and orographic Forcing. *J. Atmos. Sci*., **38**: 1179-1196.
1000 ——, and T. Ambrizzi, 1993: Rossby wave propagation on a realistic longitudinally varying
1001 flow. J. Atmos. Sci., 50, 1661-1671.
1002 ——, and G.-Y. Yang, 2016: The longitudinal variation of equatorial waves due to
1003 propagation on a zonal varying flow. *J. Atmos. Sci.*, 73, 605-620.
1004 Kiladis, G. N., C. D. Thorncroft, and N. M. J. Hall, 2006: Three dimensional structure and
1005 dynamics of African easterly waves. Part I: Observations. *J. Atmos. Sci*., **63**, 2212–2230.

1006 Landsea, C. W. ,1993, A climatology of intense (or major) Atlantic hurricanes. Mon. Weather
1007 Rev., 121, 1703– 1713.
1008 Landsea, C. W., G. D. Bell, W. M. Gray, and S. B. Goldenberg, 1998: The extremely active
1009 1995 Atlantic hurricane season: Environmental conditions and verification of seasonal
1010 forecasts. *Mon. Wea. Rev*., **126**, 1174–1193.
1011 Laurent H, d'Amato N, Lebel T,1998 How important is the contribution of the mesoscale
1012 convective complexes to the Sahelian rainfall? Phys Chem Earth 23:629–633.
1013 Liebmann, B., and C. A. Smith, 1996: Description of a complete (interpolated) outgoing
1014 longwave radiation dataset. Bull. Amer. Meteor. Soc., 77, 1275–1277.
1015 Matsuno, T., 1966: Quasi-geostrophic motions in the equatorial area. *J. Meteor. Soc. Japan*,
1016 **44,** 25–43.
1017 Mathon, V., H. Laurent, and T. Lebel,2002, Mesoscale convective system rainfall in the
1018 Sahel, J. Appl. Meteorol., 41(11), 1081–1092.Mekonnen, A., C. D. Thorncroft, and A.
1019 R. Aiyyer ,2006, Analysis of convection and its association with African easterly
1020 waves, J. Clim., 19(20), 5405–5421.
1021 Mekonnen, A., C. D. Thorncroft, and A. R. Aiyyer ,2006, Analysis of convection and its
1022 association with African easterly waves, *J. Clim*., **19** (20), 5405–5421.
1023 Molinari, J., 2004: Paradigms of tropical cyclogenesis. *Bull. Amer. Meteor. Soc*., **85**, 662-663.
1024 Nicholson, S. E., 2009: On the factors modulating the intensity of the tropical rainbelt over
1025 West Africa. *Int. J. Climatology*, **29**, 673-689.
1026 Price, C.,Y. Yair, and M. Asfur, 2007: East African lightning as a precursor of Atlantic
1027 hurricane activity. *Geophys. Res. Lett.*, 34, L09805, doi:1029/2006GL028884.
1028 Radon, J., 1917: Über die Bestimmung von Funktionen durch ihre Integralwerte längs
1029 gewisser Mannigfaltigkeiten. Math.-Phys. Kl., 69, 262–267. [For English translation see

Deans, S. R., 1983: The Radon Transform and Some of Its Applications. John Wiley and Sons, 204–217.

Reed, R. J., D. C. Norquist, and E. E. Recker, 1977: The structure and properties of African wave disturbances as observed during Phase III of GATE. *Mon. Wea. Rev.,* **105,** 317–333.

Sakai, S, 1989, Rossby-Kelvin instability: a new type of ageostrophic instability caused by a resonance between Rossby waves and gravity waves. *J. Fluid Mech*., **202**, 149-176.Schreck, C. J., J. Molinari, and A. Aiyyer, 2012: A global view of equatorial waves and tropical cyclogenesis. Mon. Wea. Rev., 140, 774–788, doi:10.1175/MWR-D-11-00110.1.

Serra, Y. L., G. N. Kiladis, and K. I. Hodges, 2010: Tracking and mean structure of easterly waves over the intra-Americas sea. *J. Climate*, 23, 4823–4840.

Takayabu, Y. N., 1994: Large scale cloud disturbances associated with equatorial waves. Part I: Spectral features of the cloud disturbances. *J. Meteor. Soc. Japan,* 72, 433–449.

Thorncroft, C. D., and M. Blackburn, 1999: Maintenance of the African easterly jet. *Quart. J. Roy. Meteor. Soc.* 125,763-786.

——, and K. I. Hodges, 2001: African easterly wave variability and its relationship to Atlantic tropical cyclone activity. *J. Climate*, **14**, 1166–1179.

Wheeler, M., and G. N. Kiladis, 1999: Convectively-coupled equatorial waves: Analysis of clouds and temperature in the wavenumber–frequency domain. J. Atmos. Sci., 56, 374–399.

——, ——, and P. Webster, 2000: Large-scale dynamical fields associated with convectively coupled equatorial waves. *J. Atmos. Sci.*, **57,** 613–640.

Yang G-Y, B. J. Hoskins, 1996: Propagation of Rossby wave of nonzero frequency. *J. Atmos. Sci.*, **53**: 2365-2378.

——, ——, 2013: ENSO impact on Kelvin waves and associated tropical convection. *J. Atmos. Sci.*, **70**, 3513-3532.

——, ——, 2016: ENSO-related variation of equatorial MRG and Rossby waves and forcing from higher latitudes. *Quart. J. Roy. Meteor. Soc.* **142**, 1488-2504.

——, ——, and J. M. Slingo, 2003: Convectively coupled equatorial waves: A new methodology for identifying wave structures in observational data. *J. Atmos. Sci*., **60**, 1637–1654.

——, ——, and ——, 2007a: Convectively coupled equatorial waves: Part I: Horizontal structure. *J. Atmos. Sci*., **64**, 3406– 3423.

——, ——, and ——, 2007b: Convectively coupled equatorial waves: Part II: Zonal propagation. *J. Atmos. Sci*., **64**, 3424–3437.

——, —— , and ——, 2007c: Convectively coupled equatorial waves: Part III: Synthesis structures and extratropical forcing. *J. Atmos. Sci*., **64**, 3438–3451.

——, —— , and ——, 2011: Equatorial waves in opposite QBO phases**.** *J. Atmos. Sci*., **68**, 839-862

——, —— , and L. Gray, 2012: The Influence of the QBO on the propagation of equatorial waves into the stratosphere. *J. Atmos. Sci*., **69**, 2959–2982.

——, J. Slingo and B.J. Hoskins, 2009: Convectively coupled equatorial waves in high resolution Hadley centre climate models. *J. Climate*, **22**, 8, 1897-1919.

Zhang, C., and P. J. Webster, 1989: Effects of zonal flows on equatorially trapped waves. *J. Atmos. Sci.*, **46,** 3632–3652.

Table 1. Climatological mean of zonal wavenumber (k), period (p) and zonal phase speed (c) of meridional wind disturbances obtained by regression onto the positive vorticity centres tracked within AEWs for the longitudinal sector centred on 0°E. Results are obtained for westward-filtered v at 12°N, 12°S and the projection of v on to WMRG waves. k and p are estimated from the regressed longitude-lag diagrams (as in Fig.11e), and c is calculated from the Radon Transform method (Radon 1917). Phase speed of vorticity centres is also indicated in square brackets.

Wave v	k (#)	p (day)	c (m s^{-1})
700-hPa v at 12°N	12-13	3-4	9.1 [8.4]
200-hPa WMRG	8-9	4-5	11.9
700-hPa WMRG	11-12	3-4	11.0
200-hPa v at 12°S	7-8	4-5	12.7

Figure Captions:

Figure 1: The horizontal structures of the normal modes for a resting atmosphere. The n=0 westward-moving mixed Rossby-gravity (WMRG) and the n=1 and 2 westward-moving Rossby (R1 and R2) waves. Vectors indicate horizontal wind and colours divergence (10^{-6} s^{-1}). The meridional trapping scale y_0 has been taken to be 6° and the zonal wave number k=12.

Figure 2: Statistics of all tracked vorticity centres at 600 hPa, passing through the region 10°W-35°E, 5°N-20°N in June-September of 1979-2010. (a) Frequency (total occurrence numbers) and (b) mean amplitude (10^{-5} s^{-1}) of positive vorticity centres. The boxes indicate 5 regions which will be used for regression. Each region spans 15° in longitude, centred at 30°W, 15°W, 0°E, 15°E and 30°E, and 10° in latitude, 8°-18°N for the two west regions and 5°-15°N for the three east regions. (c) Time series of the amplitude anomaly of the vorticity centres within all 5 regions in 1979-2010. Two dotted lines indicate one standard deviation range. There are 6 years with amplitude anomaly larger than one standard deviation: 1988, 1995, 1996, 2007, 2008 and 2010, and 6 weak years with amplitude anomaly smaller than one standard deviation: 1984, 1990, 1993, 1997, 2000 and 2002.

Figure 3: Zonal wavenumber-frequency power spectra of meridional wind, v, at 5°-18°N in the African-Atlantic sector (75°W-45°E) in June-September averaged over 1979-2010. (a) 200 hPa and (b) 700 hPa. The box indicates the broad-band filter domain used in this study and the dotted line indicates a period of 4 days.

1128 Figure 4: Longitude-height cross-section of standard deviations averaged over 1979-
1129 2010 for westward-filtered meridional wind, v (m s^{-1}), at (a) 12°N, (b) 0°N and (c) 12°S. (d)
1130 The projection of v onto WMRG structures at 0°N.
1131 Figure 5: (a) Vorticity tracks at 600hPa in JJAS 1995, with vorticity centres at 5-20°N
1132 indicated by colour circles (colour scales show intensity in 10^{-5} s^{-1}) and outside of it indicated
1133 by grey circles. (b) 700-hPa WMRG v (m s^{-1}) at 0°N with vorticity centres at 5-20°N
1134 superimposed. `F' in each panel indicates hurricane `Felix'.
1135 Figure 6: Horizontal winds at 700 hPa, for (a) westward-filtered component and (b) the
1136 WMRG wave structure, during 4-9 August 1995. The red circles indicate positive vorticity
1137 centres and are sized in accordance with the amplitude of the vorticity (10^{-5} s^{-1}). `A', `B' and
1138 'C' indicate three vorticity centres.
1139 Figure 7: As in Fig.6 but for 200 hPa westward-filtered winds and WMRG waves.
1140 Fig.8: Horizontal winds regressed onto vorticity centres in the region centred at 0°E.
1141 (a) 700 hPa westward-filtered winds, (b) 700 hPa WMRG waves and (c) 200 hPa WMRG
1142 waves. The relative longitude axis is 0 at the location of the positive AEW vorticity centre.
1143 Red regions are auto-regressed vorticity centres, sized in accordance with the amplitude of the
1144 vorticity with a unit of 10^{-5} s^{-1}. Only those vectors with the u or v exceeding the 95%
1145 significance level are shown.
1146 Figure 9: Longitude-height cross-sections for meridional wind regressed onto AEW
1147 vorticity centres in 5 regions, centred at 30°W, 15°W, 0°E, 15°E and 30°E. (a) Westward-
1148 filtered v at 12°N, (b) the equatorial Rossby wave structures R1 plus R2 at 12°N, (c) WMRG
1149 waves at 0°N and (d) westward-filtered v at 12°S. Each panel shows longitude relative to the
1150 vorticity centres that pass through the region. The solid (dotted) lines indicate positive
1151 (negative) values. In (a), (b) contours start at +/- 0.2, with an interval of 0.4 m s^{-1}. In (c) and

(d) contours are halved. In the shaded areas, regressed values exceed the 95% significance level.

Figure 10: Longitude-height cross-section of standard deviations in meridional wind (m s^{-1}) averaged for (left) 6 strong, (middle) 6 weak AEW years, and (right) the difference between them. Westward-filtered *v* at (a) 12°N, (b) 0°N and (c) 12°S and (d) WMRG at 0°N. In the difference fields, the shaded areas denote values exceeding the 95% significance level (given variability between years).

Figure 11: Fields regressed onto AEW vorticity centres in the region centred on 0°E, averaged for (left) climatology, (middle) 6 strong and (right) 6 weak AEW years. (a) 200-hPa westward-filtered winds. (b) 200 hPa WMRG structures. (c) Vorticity stretching by the WMRG component averaged over 5-18°N (units 10^{-11} s^{-2}). (d) Lag-height diagram of WMRG equatorial *v*, with the AEW vorticity centre located at day 0. Solid (dotted) lines indicate positive (negative) values with a contour interval of 0.3 m s^{-1}. (e) Longitude-lag diagram of 200-hPa WMRG equatorial *v*. Red circles are auto-regressed vorticity centres (unit of 10^{-5} s^{-1}). In (a), (b), (c) and (e) only winds exceeding the significance level of 95% are shown. In (d) the shaded areas denote regions of regressed values exceeding the 95% significance level.

Figure 12: Westward-filtered OLR (colour, W m^{-2}) and horizontal winds at (a) 200 hPa and (b) 700 hPa in strong AEW years, regressed onto vorticity centres in two regions centred at (left) 15°W and (right) 0°E. Other conventions are as in Fig. 8. Only winds exceeding the 95% significance level are shown.

Figure 13: Zonal winds averaged over (a) the upper troposphere (200-300 hPa) and (b) lower troposphere (600-700 hPa). Composite for (left) six strong AEW years, (middle) six weak AEW years and (right) difference between them, over the African-Atlantic sector. The contour interval is 4 m s^{-1} in (a) and 2 m s^{-1} in (b). The shading area in the difference fields indicates the difference values exceeding the 95% significance level.

1177 Figure 14: Basic flow and diagnosis of WMRG and RW propagation at 200-300 hPa
1178 in the sector 75°W-45°E. (a) U (solid, m s^{-1}) and β (dotted, $5*10^{-12}$ m^{-1} s^{-1}) for years of strong
1179 (black) and weak (grey) AEW activity. (b) Dispersion curves for WMRG (solid), R1 (dashed),
1180 and Kelvin (dotted) waves, using c_e=20 m s^{-1}, planetary β_0=$2.28*10^{-11}$ m^{-1} s^{-1} and U (averaged
1181 over 12°N-12°S) in strong (black) and weak (grey) AEW years. (c)-(d) Rossby wave
1182 propagation diagnosed for period = - 4 days using observed zonal wind profiles in (c) strong
1183 and (d) weak AEW years. Thick solid lines indicate reflection wavenumbers and the dotted
1184 line indicates critical wavenumber. Permitted wave numbers for RW propagation are shaded.
1185 (e)-(f) Phase speeds (m s^{-1}) of RW (solid, c_2) along k_2 line defined in Eq. (7) and WMRG
1186 (dotted, c_2-MRG) calculated from Eq. (9) using the k_2 with β_0 and U_0 in (e) strong and (f)
1187 weak AEW years.
1188 Figure 15: Horizontal winds (with only the time mean and zonal mean removed)
1189 regressed onto 200-hPa WMRG minimum in v (northerlies) in the region centred on 15°W
1190 spanning 30° longitude at lag day -1. (a) 6 strongest and (b) 6 weakest AEW years. (c)
1191 Horizontal momentum flux [u^*v^*] of full winds, averaged over -64° to 80° (two wavelengths)
1192 for strong (solid) and weak (dotted) AEW years (units m^2 s^{-2}). Only values exceeding the 95%
1193 significance level are shown in (a) and (b).

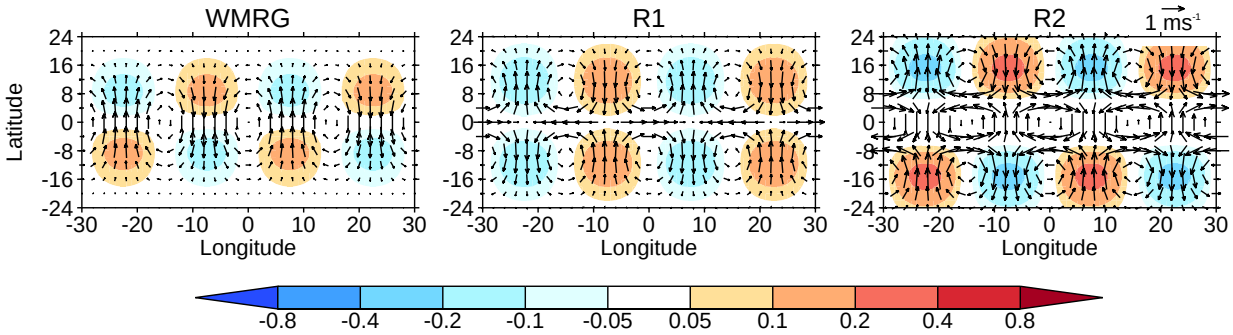

Fig.1 The horizontal structures of the normal modes for a resting atmosphere. The n=0 westward-moving mixed Rossby-gravity (WMRG) and the n=1 and 2 westward-moving Rossby (R1 and R2) waves. Vectors indicate horizontal wind and colours divergence (s^{-1}). The meridional scale y_0 has been taken to be 6^o and the zonal wave number k=12.

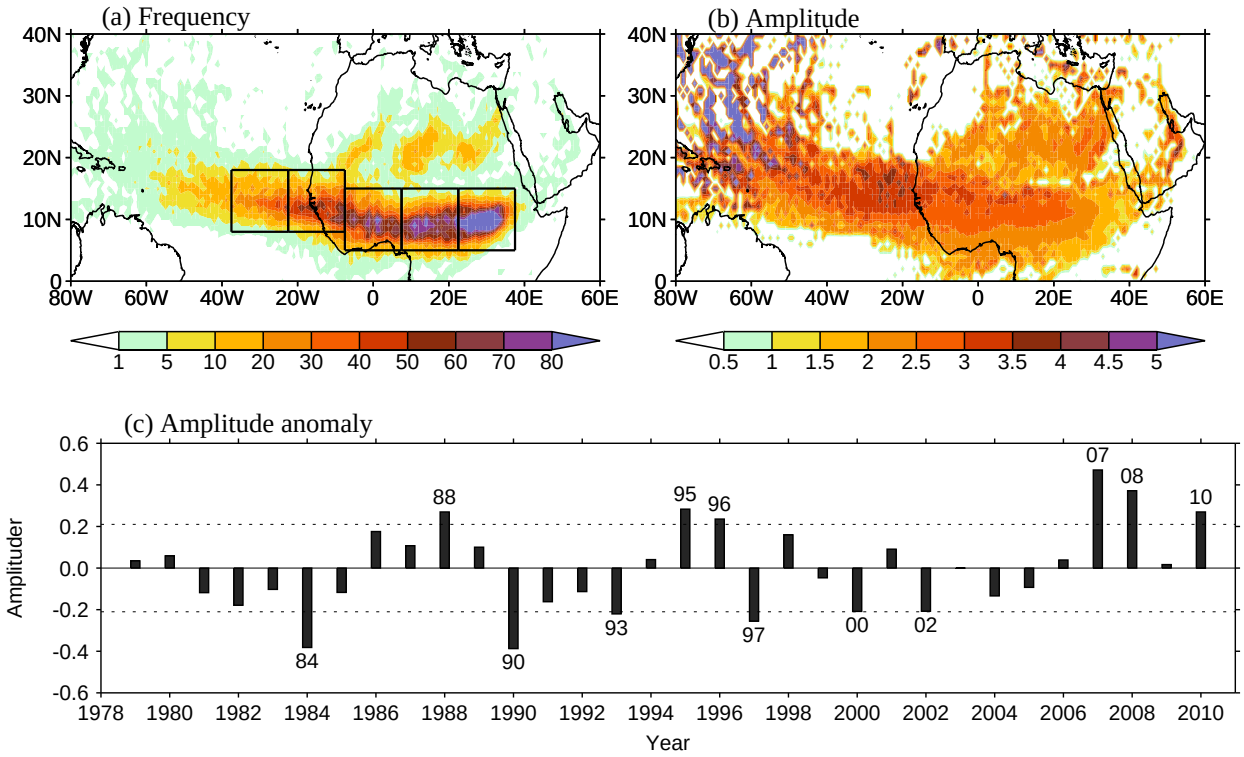

Fig.2 Statistics of all tracked vorticity centres at 600 hPa, passing through the region 10^{o}W-35^{o}E, 5^{o}N-20^{o}N in June-September of 1979-2010. (a) Frequency (total occurrence numbers) and (b) mean amplitude (10^{-5} s^{-1}) of positive vorticity centres. The boxes indicate 5 regions which will be used for regression. Each region spans 15^{o} in longitude, centred at 30^{o}W, 15^{o}W, 0^{o}E, 15^{o}E and 30^{o}E, and 10^{o} in latitude, 8^{o}-18^{o}N for the two west regions and 5^{o}-15^{o}N for the three east regions. (c) Time series of the amplitude anomaly of the vorticity centres within all 5 regions in 1979-2010. Two dotted lines indicate one standard deviation range. There are 6 years with amplitude anomaly larger than one standard deviation: 1988, 1995, 1996, 2007, 2008 and 2010, and 6 weak years with amplitude anomaly smaller than one standard deviation: 1984, 1990, 1993, 1997, 2000 and 2002.

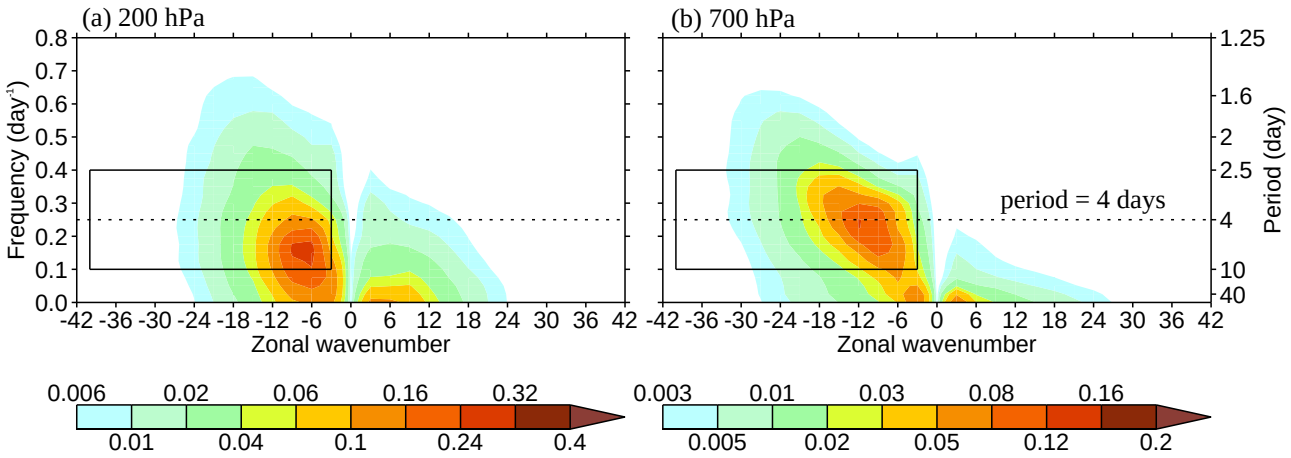

Figure 3 Zonal wavenumber-frequency power spectra of meridional wind, *v*, at 5^{o}-18^{o}N in the African-Atlantic sector (75^{o}W-45^{o}E) in June-September averaged over 1979-2010. (a) 200 hPa and (b) 700 hPa. The box indicates the broad-band filter domain used in this study and the dotted line indicates a period of 4 days.

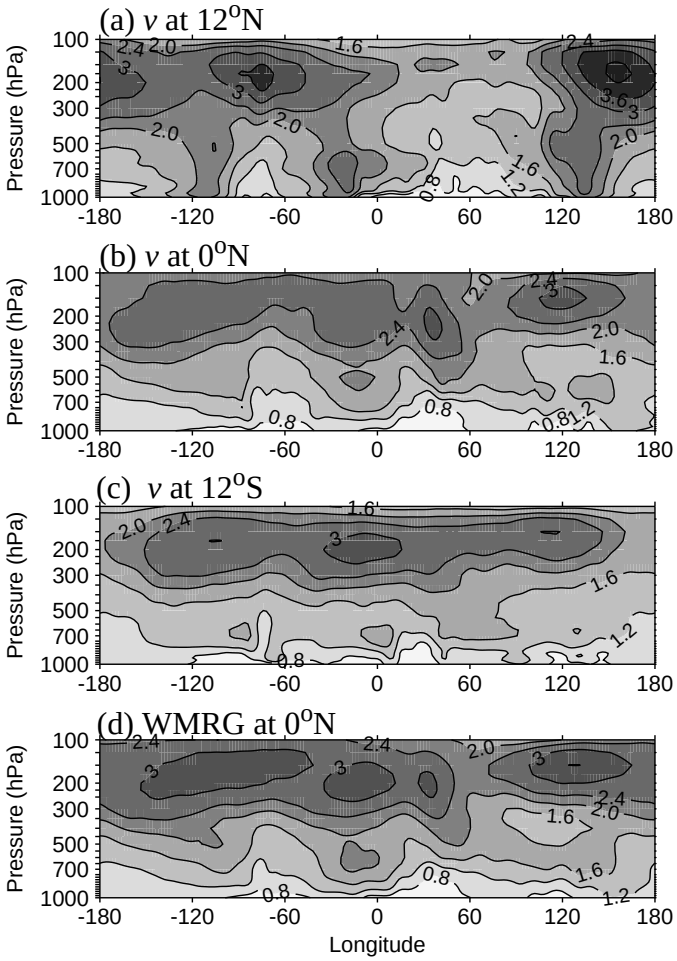

Figure 4 Longitude-height cross section of standard deviations averaged over 1979-2010 for westward-filtered meridional wind v (m s^{-1}), at (a) 12°N, (b) 0°N and (c) 12°S. (d) The projection of v onto WMRG structures at 0°N.

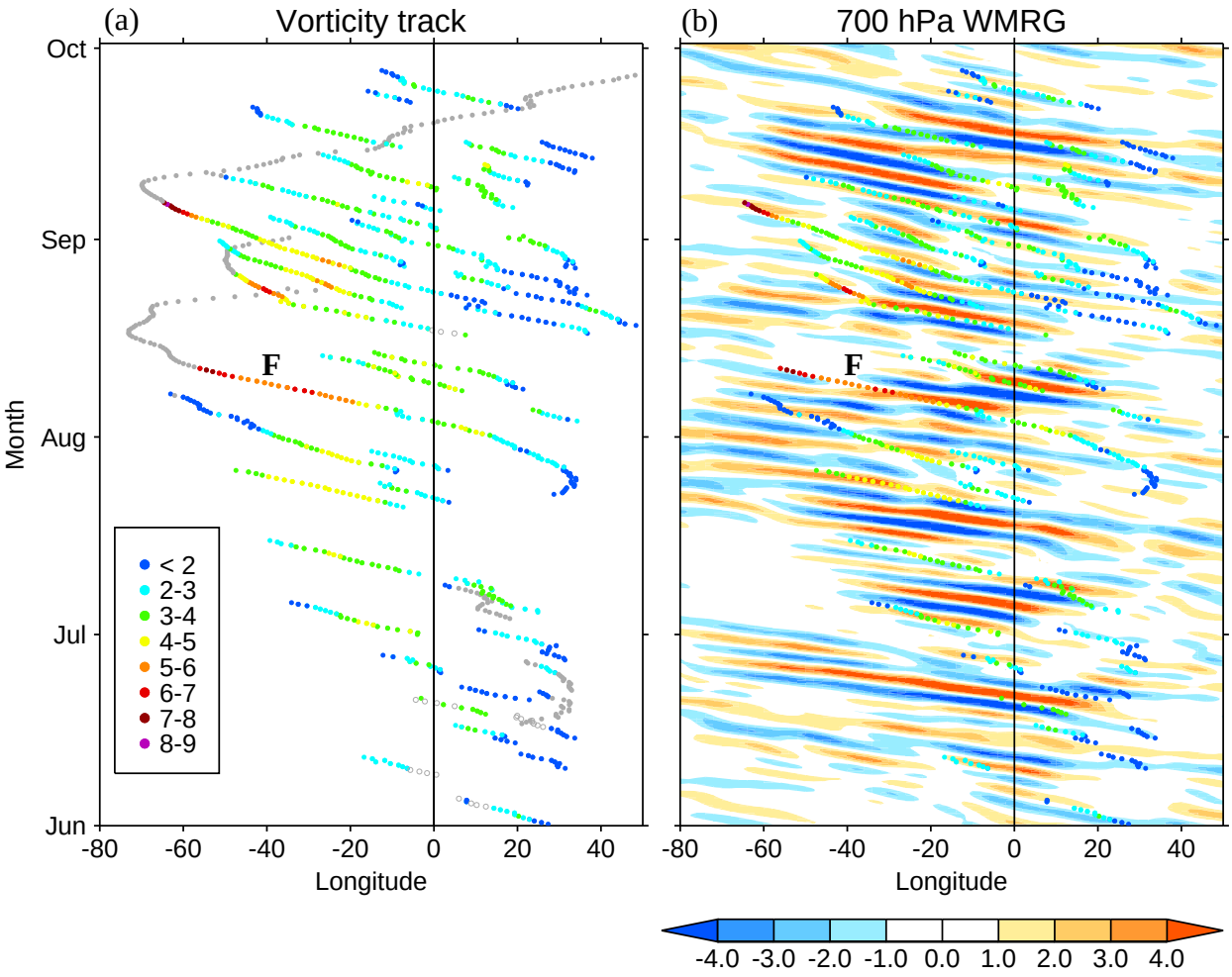

Figure 5 (a) Vorticity tracks at 600 hPa in JJAS 1995, with vorticity centres at 5-20^{o}N indicated by colour circles (colour scales show intensity in 10^{-5} s^{-1}) and outside of it indicated by grey circles. (b) 700-hPa WMRG *v* (m s^{-1}) at 0^{o}N with vorticity centres at 5-20^{o}N superimposed. 'F' in each panel indicates hurricane 'Felix'.

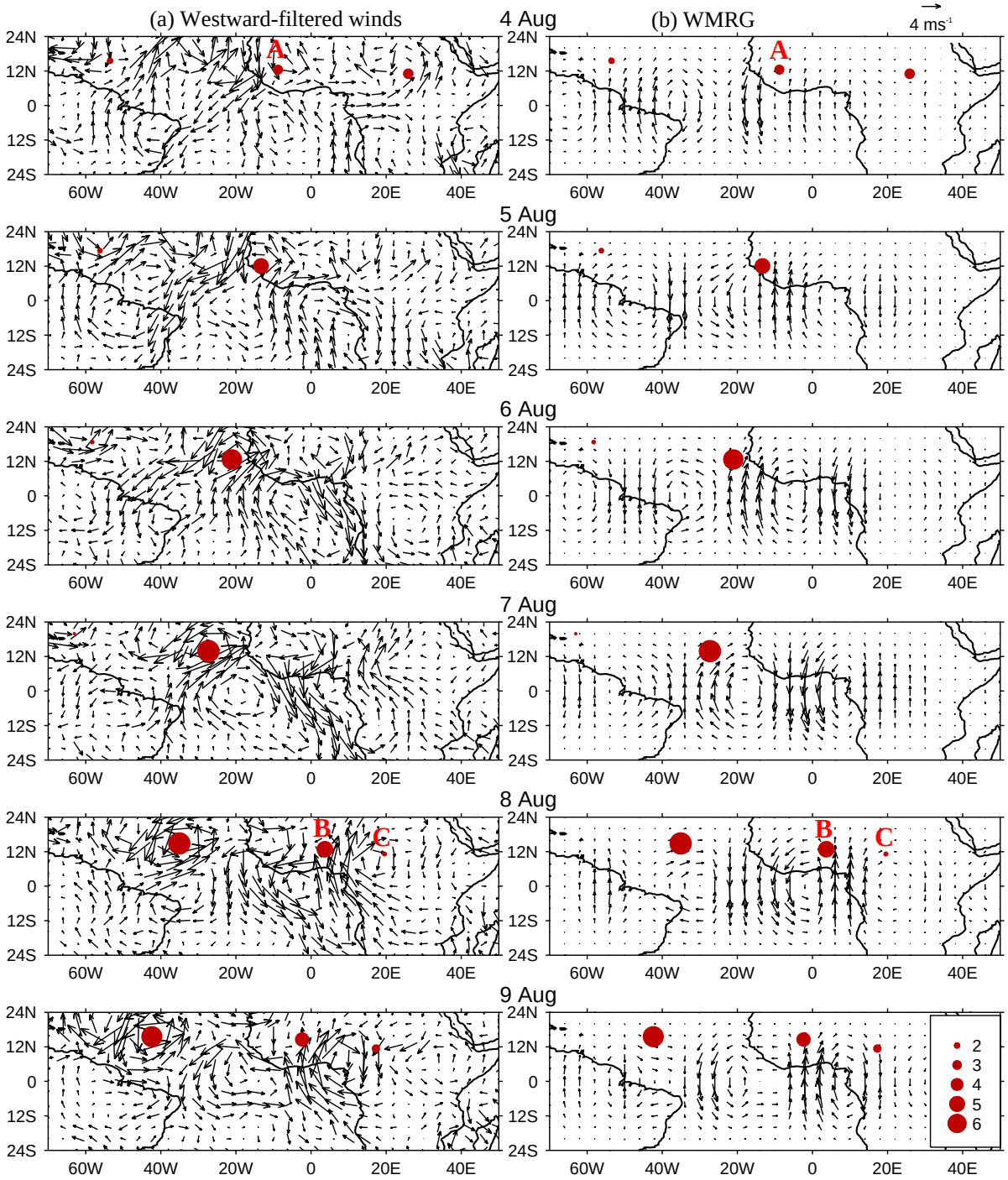

Figure 6 Horizontal winds at 700 hPa, for (a) westward-filtered component and (b) the projection onto WMRG wave structure, during 4-9 August 1995. The red circles indicate positive vorticity centres and are sized in accordance with the amplitude of the vorticity($10^{-5}s^{-1}$). 'A', 'B' and 'C' indicates three vorticity centres.

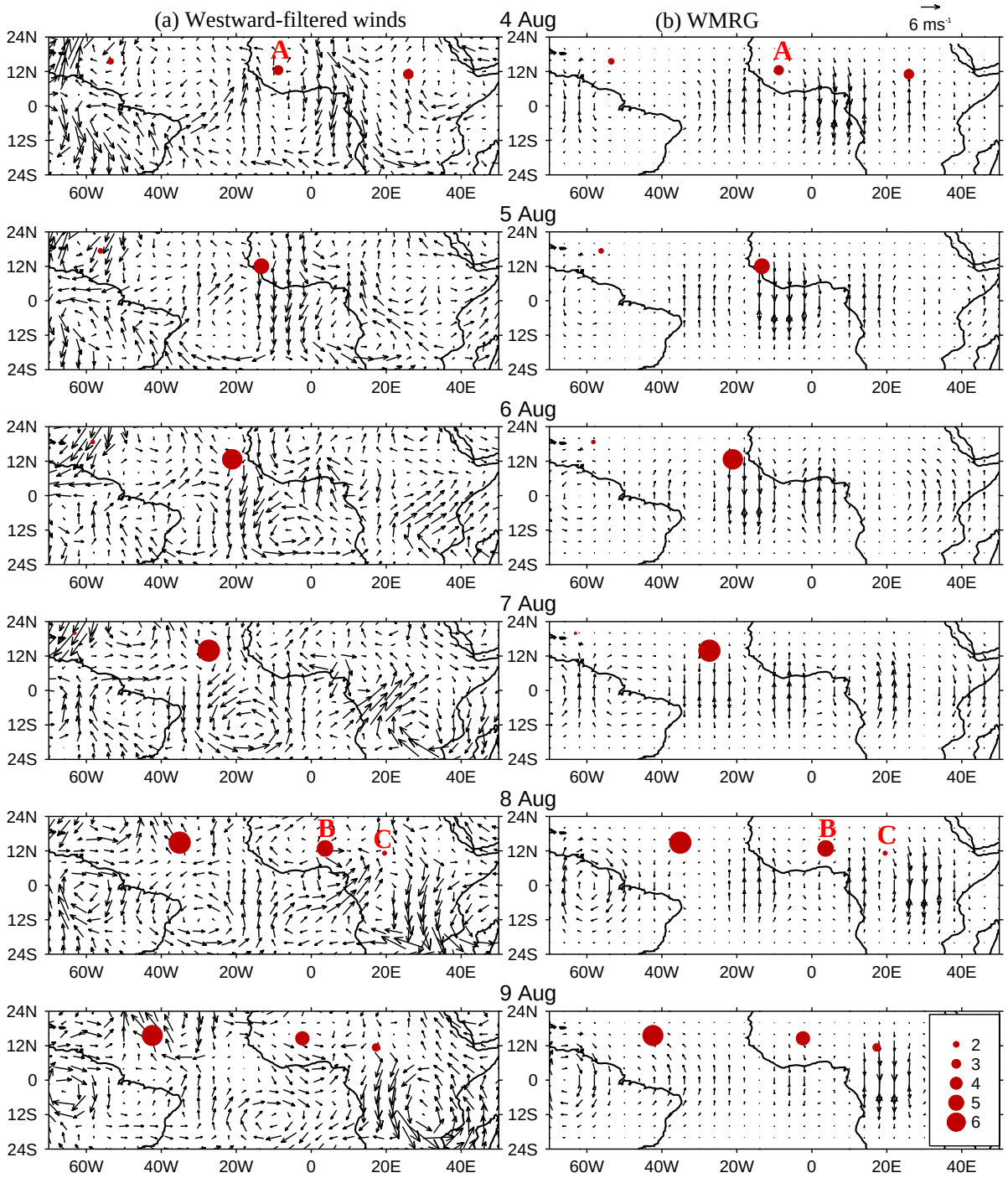

Figure 7 As in Fig.6 but for 200-hPa westward-filtered winds and projection onto WMRG waves.

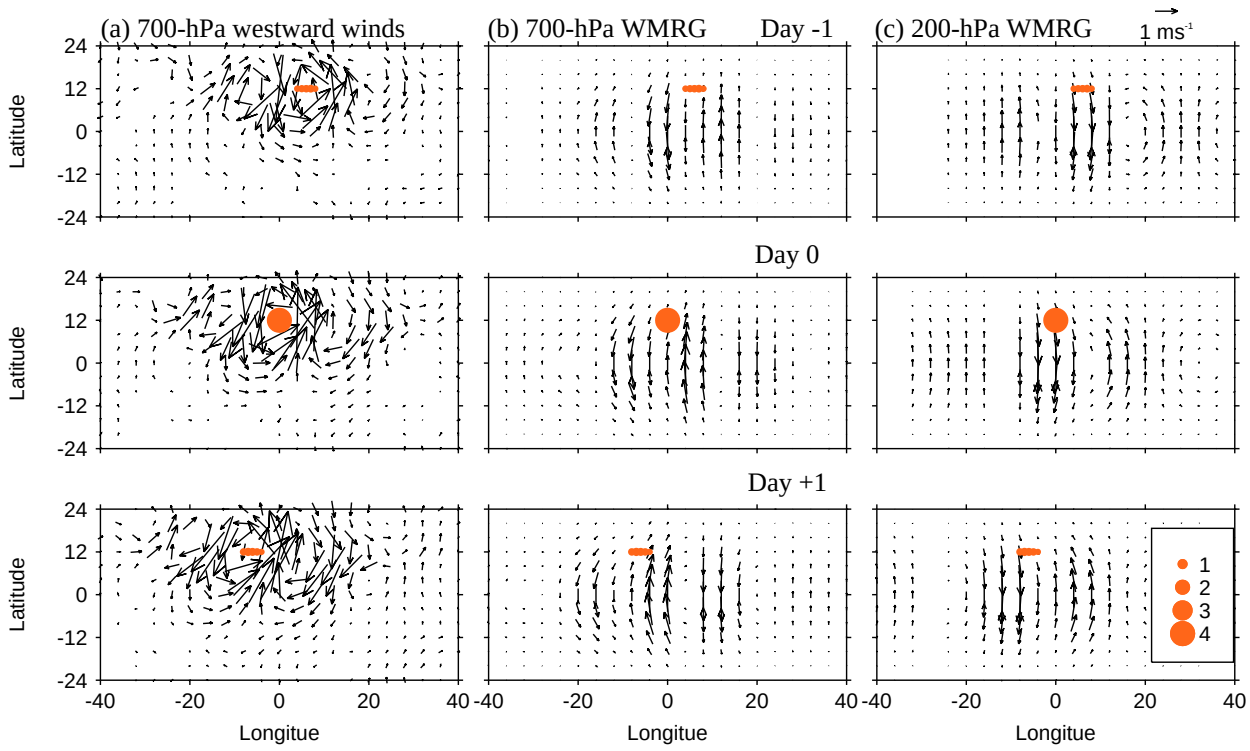

Figure 8 Horizontal winds regressed onto vorticity centres in the region centred at 0^{o}E. (a) 700-hPa westward-filtered winds, (b) 700 hPa projection onto WMRG waves and (c) 200 hPa WMRGwaves.The relative longitude axis is 0 at the location of the positive AEW vorticity centre. Red regions are auto-regressed vorticity centres, sized in accordance with the amplitude of the vorticity with a unit of 10^{-5} s^{-1}. Only those vectors with the *u* or *v* exceeding the 95% significance level are shown.

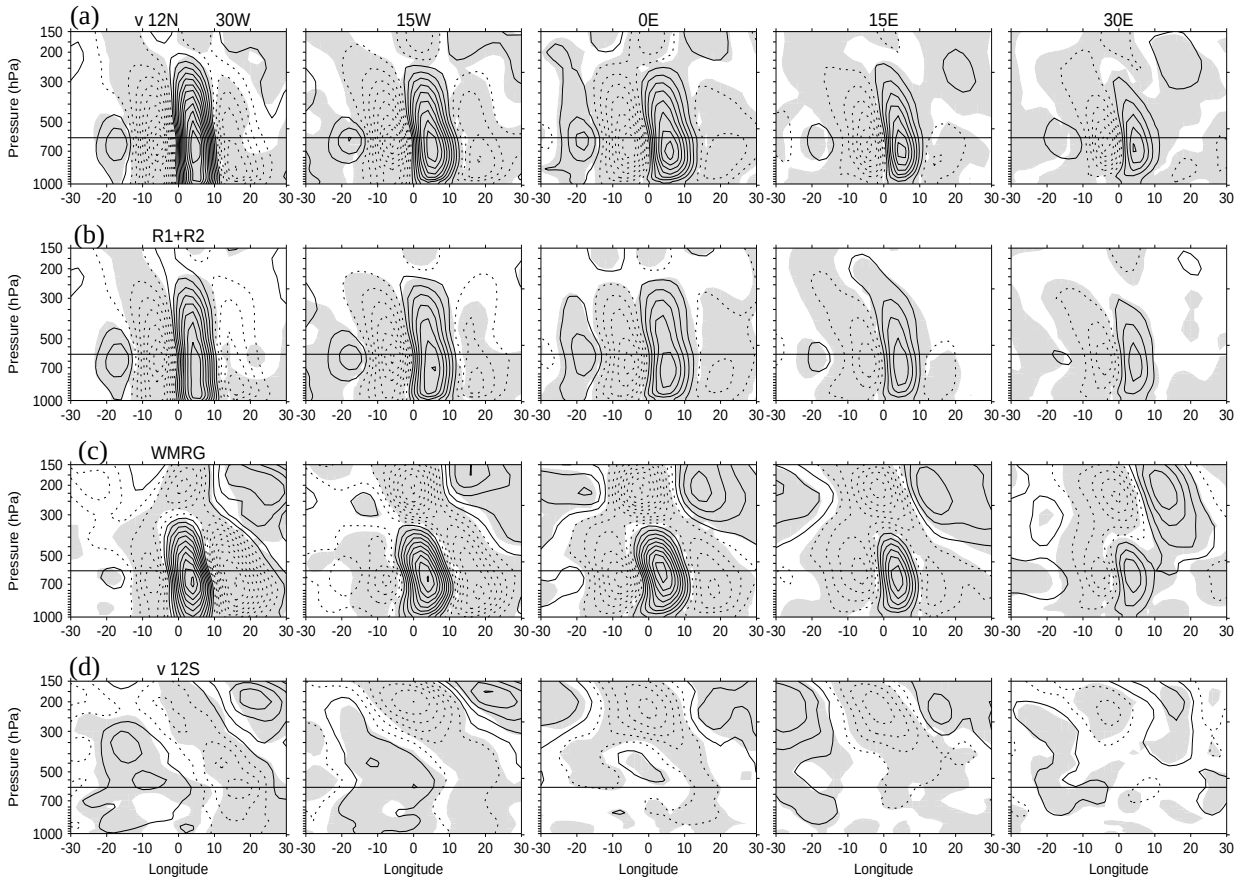

Figure 9 Longitude-height cross-sections for meridional wind regressed onto AEW vorticity centres in 5 regions, centred at 30^{o}W,15^{o}W, 0^{o}E,15^{o}E and 30^{o}E. (a) westward-filtered *v* at 12^{o}N,(b) projection of *v* onto the equatorial Rossby wave structures R1 plus R2 at 12^{o}N, (c) projection onto WMRG wave at 0^{o}N and (d) westward-filtered *v* at 12^{o}S. Each panel shows longitude relative to the vortcity centres that pass through the region. The solid (dotted) lines indicate positive (negative) values.In (a), (b) contours start at +/- 0.2, with an interval of 0.4 m s^{-1}. In (c) and (d) contours are halved. In the the shaded areas regressed values exceed the 95% significance level.

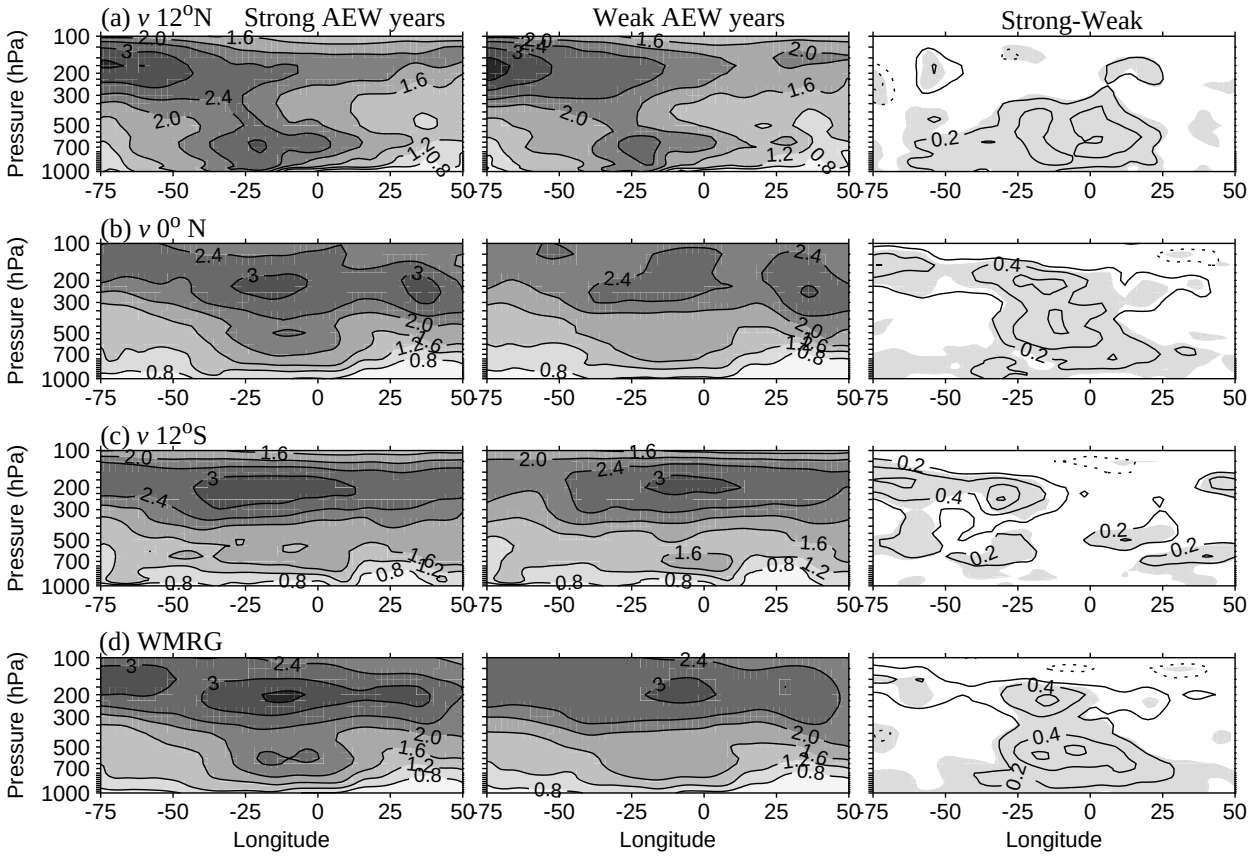

Figure 10 Longitude-height cross-section of standard deviations in meridional wind (m s^{-1}) averaged for (left) 6 strong, (middle) 6 weak AEW years, and (right) the difference between them. Westward-filtered *v* at (a) 12°N, (b) 0°N and (c) 12°S and (d) projection of *v* onto WMRG structures. In the difference fields, the shaded areas denote values exceeding the 95% significance level (given variability between years)

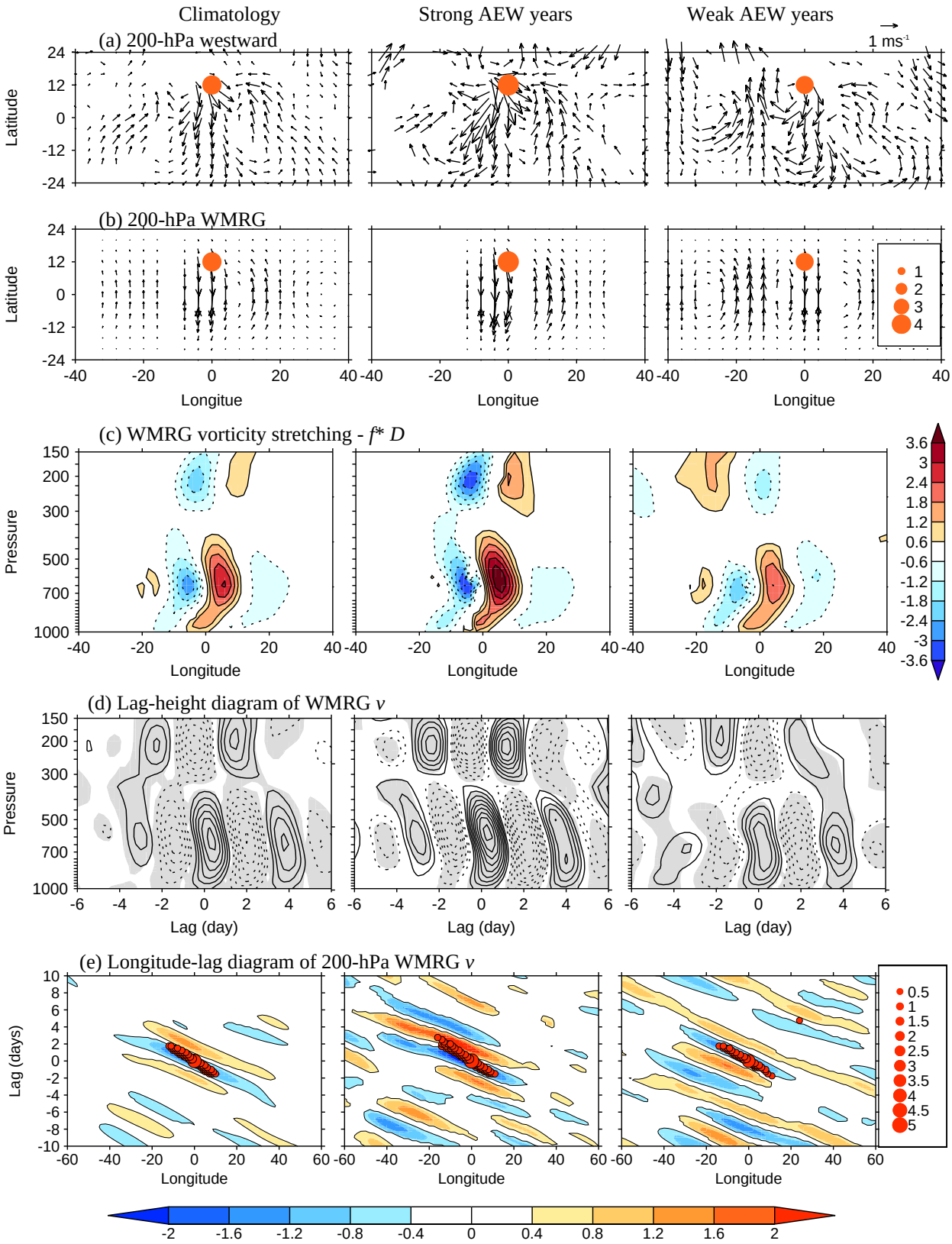

Figure 11 Fields regressed onto AEW vorticity centres in the region centred on 0°E, averaged for (left) climatology, (middle) 6 strong and (right) 6 weak AEW years. (a) 200-hPa westward-filtered winds. (b) 200 hPa projection onto WMRG structures. (c) Vorticity stretching by the WMRG component averaged over 5-18°N (units 10^{-11} s^{-2}). (d) Lag-height diagram of WMRG equatorial *v*, with the AEW vorticity centre located at day 0. Solid (dotted) lines indicate positive (negative) values with a contour interval of 0.3 m s^{-1}. (e) Longitude-lag diagram of 200-hPa WMRG equatorial *v*. Red circles are auto-regressed vorticity centres (unit of 10^{-5} s^{-1}). In (a), (b), (c) and (e) only winds exceeding the significance level of 95% are shown. In (d) the shaded areas denote regions of regressed values exceeding the 95% significance level.

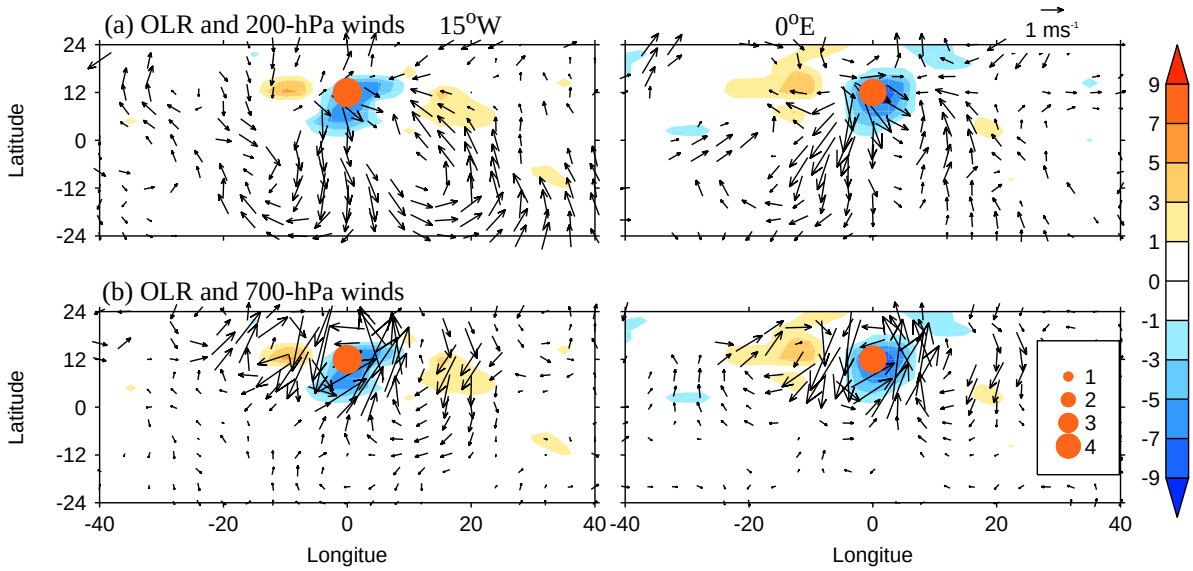

Figure 12 Westward-filtered OLR (colour, Wm^{-2}) and horizontal winds at (a) 200 hPa and (b) 700 hPa in strong AEW years, regressed onto vorticity centres in two regions centred at (left) 15°W and (right) 0°E. Other conventions are as in Fig. 8. Only winds exceeding the 95% significance level are shown.

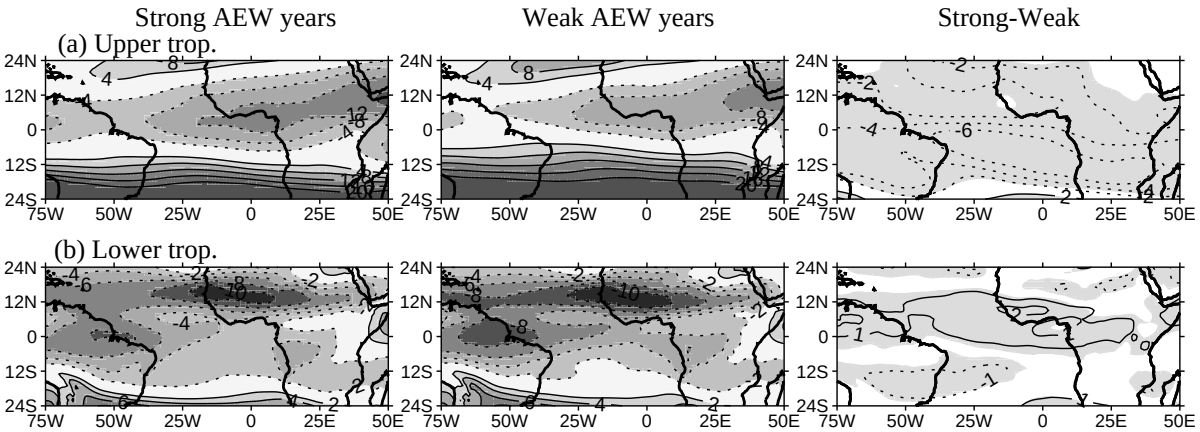

Figure 13 Zonal winds averaged over (a) the upper troposphere (200 -300 hPa) and (b) lower troposphere (600-700 hPa). Composite for (left) six strong AEW years, (middle) six weak AEW years and (right) difference between them, over the African-Atlantic sector. The contour interval is 4 m s^{-1} in (a) and 2 m s^{-1} in (b). The shaded areas in the difference fields indicate the differentce values exceeding the 95% significance level.

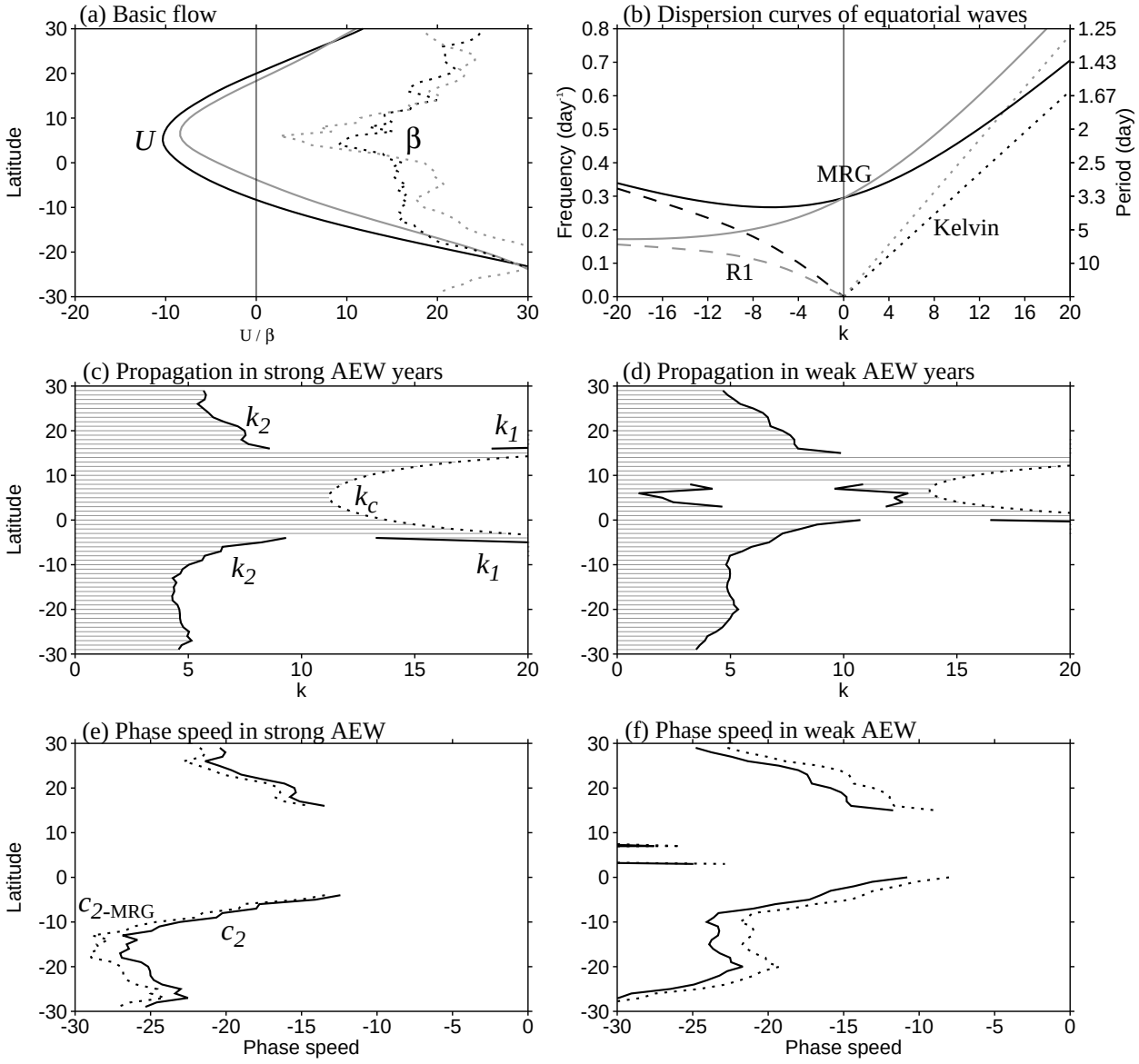

Figure 14 Basic flow and diagnosis of WMRG and RW propagation at 200-300 hPa in the sector 75°W-45°E. (a) U (solid, m s^{-1}) and β (dotted, $5*10^{-12}$ m^{-1} s^{-1}) for years of strong (black) and weak (grey) AEW activity. (b) Dispersion curves for WMRG (solid), R1(dashed), and Kelvin (dotted) waves, using c_e=20 m s^{-1}, planetary $\beta_0=2.28*10^{-11}$ m^{-1} s^{-1} and U (averaged over 12°N-12°S) in strong (black) and weak (grey) AEW years. (c)-(d) Rossby wave propagation diagnosed for period =-4 days using observed zonal wind profiles in (c) strong and (d) weak AEW years. Thick solid lines indicate reflection wavenumbers and the dotted line indicates critical wavenumber. Permitted wave numbers for RW propagation are shaded. (e)-(f) Phase speeds (m s^{-1}) of Rossby waves (Solid, c_2) along k_2 line defined in Eq. (7) and WMRG (dotted, c_2-MRG) calculated from Eq. (9) using the k_2 with β_0 and U_0 in (e) strong and (f) weak AEW years.

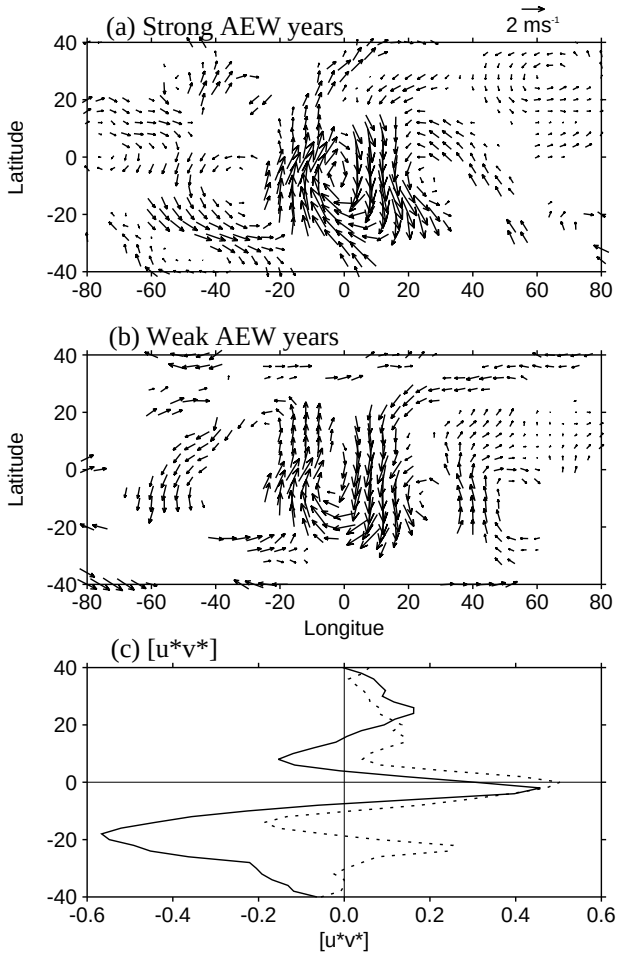

Figure 15 Horizonatl winds (with only the time mean and zonal mean removed) regressed onto 200-hPa WMRG minimum in v (northerlies) in the region centred on 15^{o}W spanning 30^{o} longitudes at lag day -1. (a) 6 strongest and (b) 6 weakest AEW years. (c) Horizontal momentum flux [u*v*] of full winds, averaged over -64^{o} to 80^{o} (two wave-lengths) for strong (solid) and weak (dotted) AEW years (units m^{2} s^{-2}). Only values exceeding the 95% significance level are shown in (a) and (b).